STUK-TR 23 / AUGUST 2016

TR

Hydraulic head responses to induced disturbances: Implications for models of sparsely-fractured rock at Olkiluoto

Joel Geier

Säteilyturvakeskus
Strålsäkerhetscentralen
Radiation and Nuclear Safety Authority
STUK

STUK-TR 23 / AUGUST 2016

Hydraulic head responses to induced disturbances: Implications for models of sparsely-fractured rock at Olkiluoto

Joel Geier
Clearwater Hardrock Consulting

Responsible in STUK has been Ari Luukkonen

STUK • **SÄTEILYTURVAKESKUS**
STRÅLSÄKERHETSCENTRALEN
RADIATION AND NUCLEAR SAFETY AUTHORITY

Osoite/Address • Laippatie 4, 00880 Helsinki
Postiosoite / Postal address • PL / P.O.Box 14, FIN-00881 Helsinki, FINLAND
Puh./Tel. (09) 759 881, +358 9 759 881 • Fax (09) 759 88 500, +358 9 759 88 500 • www.stuk.fi

The conclusions presented in the STUK report series are those of the authors and do not necessarily represent the official position of STUK.

ISBN 978-952-309-333-1 (print, Erweko Oy, Helsinki/Finland 2016)
ISBN 978-952-309-334-8 (pdf)
ISSN 1796-7171

GEIER Joel (Clearwater Hardrock Consulting). Hydraulic head responses to induced disturbances: Implications for models of sparsely-fractured rock at Olkiluoto. STUK-TR 23. Helsinki 2016. 35 pp + Appendices 16 pp.

Keywords: radioactive waste, groundwater flow, sparsely fractured rock, well-test analysis, generalized radial flow

Abstract

Responses to hydraulic disturbances at Olkiluoto were examined for indications as to the appropriateness of the model for the sparsely fractured rock, in the site descriptive model. Time-dependent drawdowns of hydraulic head in response to pumping tests were evaluated using the generalized radial flow concept, to assess whether the apparent flow dimensions observed were consistent with a well-connected discrete-fracture network model, or whether a more sparsely connected model is required.

The results generally indicate that flow between observation intervals with direct connections via hydrogeological zones are close to cylindrical (2-D), although with variability that may reflect local heterogeneity in those zones. Observation intervals without direct connections via hydrogeological zones tend to exhibit higher flow dimensions, indicative of more spherically divergent flow systems in the sparsely-fractured rock. On the three different scales of cross-hole tests considered, the preponderance of results point toward a well-connected flow system that tends toward 2-D or 3-D behavior. However the occurrence of sub-cylindrical flow in the highest-conductivity cases gives support to the idea that the strongest flow paths in the sparsely fractured rock are also sparsely connected.

One model of the sparsely-fractured rock that could account for both these types of behavior is a well-connected network of mostly low-transmissivity fractures, within which there are a few persistent, higher-conductivity channels.

GEIER Joel (Clearwater Hardrock Consulting). Hydrauliset painekorkeusvasteet aiheutetuissa häiriökentissä: päätelmiä harvaan rakoilleen kallion ominaisuuksista Olkiluodossa. STUK-TR 23. Helsinki 2016. 35 s + liiteet 16 s.

Avainsanat: radioaktiivinen jäte, pohjavesivirtaus, harvaan rakoillut kallio, hydrogeologinen vuorovaikutusanalyysi, yleistetty radiaalin virtauksen malli

Tiivistelmä

Työssä tulkittiin Olkiluodossa tehtyjen hydraulisten vuorovaikutuskokeiden painekorkeusvasteita ja pyrittiin tulkitsemaan paikkamallissa esitetyn harvaan rakoilleen kallion mallin oikeellisuutta. Pumppauskokeiden ajasta riippuvia hydraulisia painekorkeuden alenemia arvioitiin yleistetyllä radiaalisen virtauksen mallilla. Mallinnuksien tarkoituksena oli arvioida ovatko näennäiset havaitut virtausdimensiot yhtäpitäviä hydraulisesti hyvin kytkeytyneen kallion rakoverkoston mallin kanssa vai tulisiko kalliota kuvata jollakin vähemmän hydraulisesti kytkeytyneellä mallilla.

Yleisesti ottaen tulokset viittaavat siihen, että suoria yhteyksiä sisältävillä havaintoväleillä hydrogeologisten vyöhykkeiden virtauskentät ovat lähes sylinterisymmetrisiä (2-D), vaikka tulosten vaihteluväli viittaa myös vyöhykkeiden paikalliseen heterogeenisuuteen. Havaintovälit, joita ei voi tulkita hydrogeologisten vyöhykkeiden välisillä suorilla yhteyksillä, viittaavat pikemminkin korkeampiin pallosymmetrisille virtauskentille ominaisiin dimensioihin harvaan rakoilleessa kalliossa. Kolmessa eri mittakaavassa tulkittujen reikien välisten vuorovaikutuskokeiden perusteella enemmistö tuloksista indikoi hydraulisesti hyvin kytkeytyneitä 2-D tai 3-D virtausjärjestelmiä. Toisaalta alempien virtausdimensioiden esiintyminen rakenteissa, joihin on liitetty suurimmat vedenjohtavuudet, tukevat ajatusta siitä, että virtausvolyymiltään suurimmat virtausreitit harvaan rakoilleessa kalliossa ovat myös vähemmän kytkeytyneitä.

Harvaan rakoilleen kallion malli, joka pystyisi huomioimaan molemmat havaitut piirteet, voisi olla esimerkiksi hyvin kytkeytynyt enimmäkseen alhaisen transmissiviteetin rakoverkosto, johon on lisätty joitakin jatkuvia hyvin johtavia kanavia.

Contents

1 Introduction

The main goal of this evaluation is to check whether the hydraulic responses observed by Posiva's monitoring program at Olkiluoto are consistent with the site descriptive model based on a site-scale flow network that consists of essentially two-dimensional, relatively conductive hydrogeological zones (HZs) and a discrete-fracture network (DFN) model of the intervening rock, based on equidimensional fractures.

The approach is to examine time-dependent drawdowns of hydraulic head in response to pumping tests and other identifiable hydraulic disturbances, to evaluate whether the system is over-connected or under-connected relative to what should be expected based on Posiva's conceptual model. Evidence of an under-connected system would favor consideration of alternative models such as sparse channel-network models, which have been suggested as a possibility in STUK's prior review (Chapman et al., 2015). Conversely evidence of an over-connected system could support the use of equivalent-continuum modeling approaches.

The hydrogeological monitoring program at Olkiluoto includes the deep surface-based drillholes, OL-KR1 through OL-KR57 (Figure 1.1), some of which have associated shallower drillholes that were drilled from the same drilling site, and have the letter “B” appended to the name (for example, OL-KR15B through OL-KR18B as indicated in Figure 1.1) . In addition, a number of drillholes have been drilled from the ONKALO underground facility as shown in Figure 1.2, which have been used for groundwater pressure monitoring.

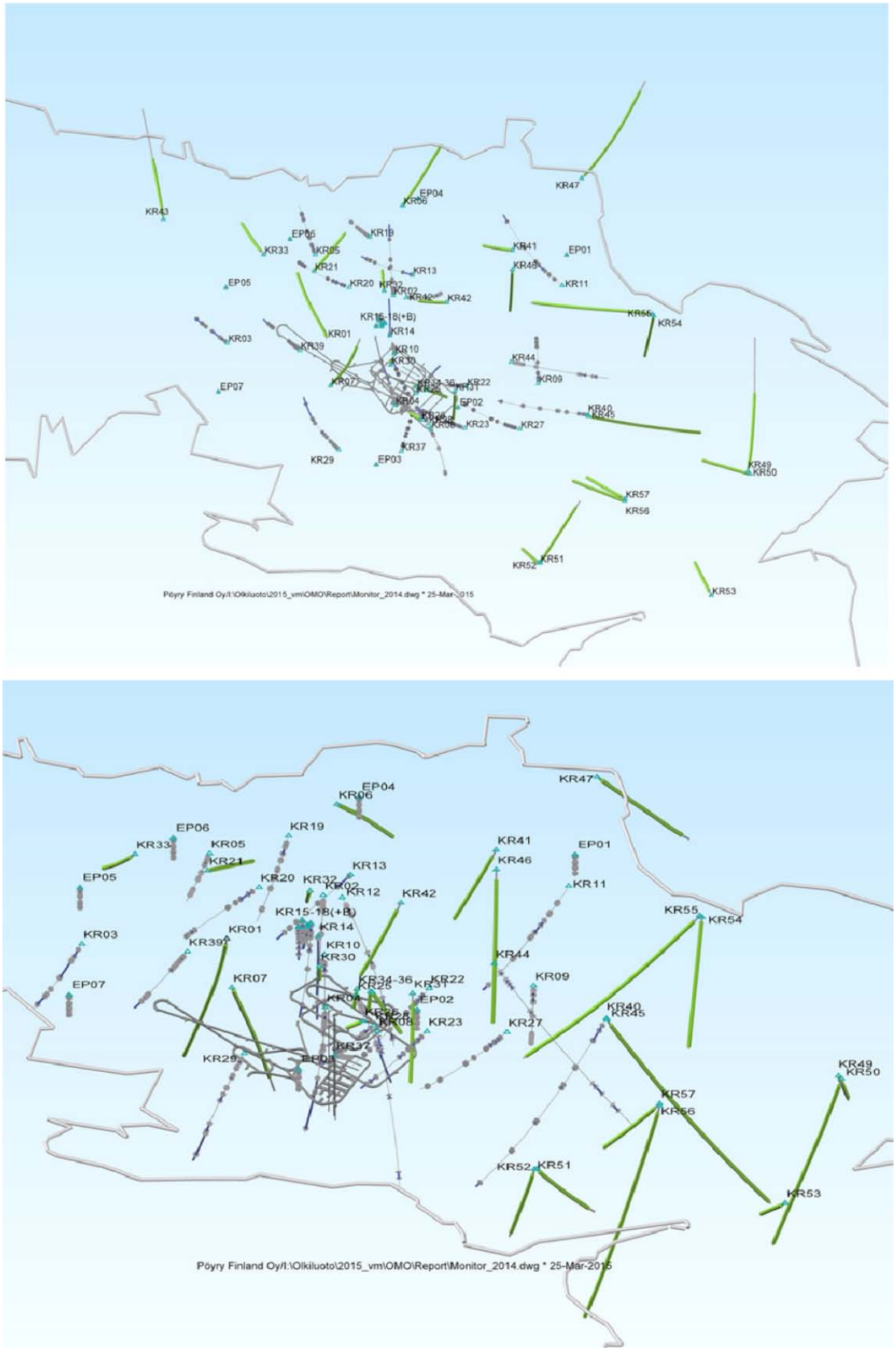

Figure 1.1. The network for observations of head or water level in packed-off drillholes (blue sections), multi-level piezometers and deep open drillholes (green) on Olkiluoto at the end of 2014. View from above (upper) and towards north (lower). From Vaittinen et al. (2015, Figure 3-5).

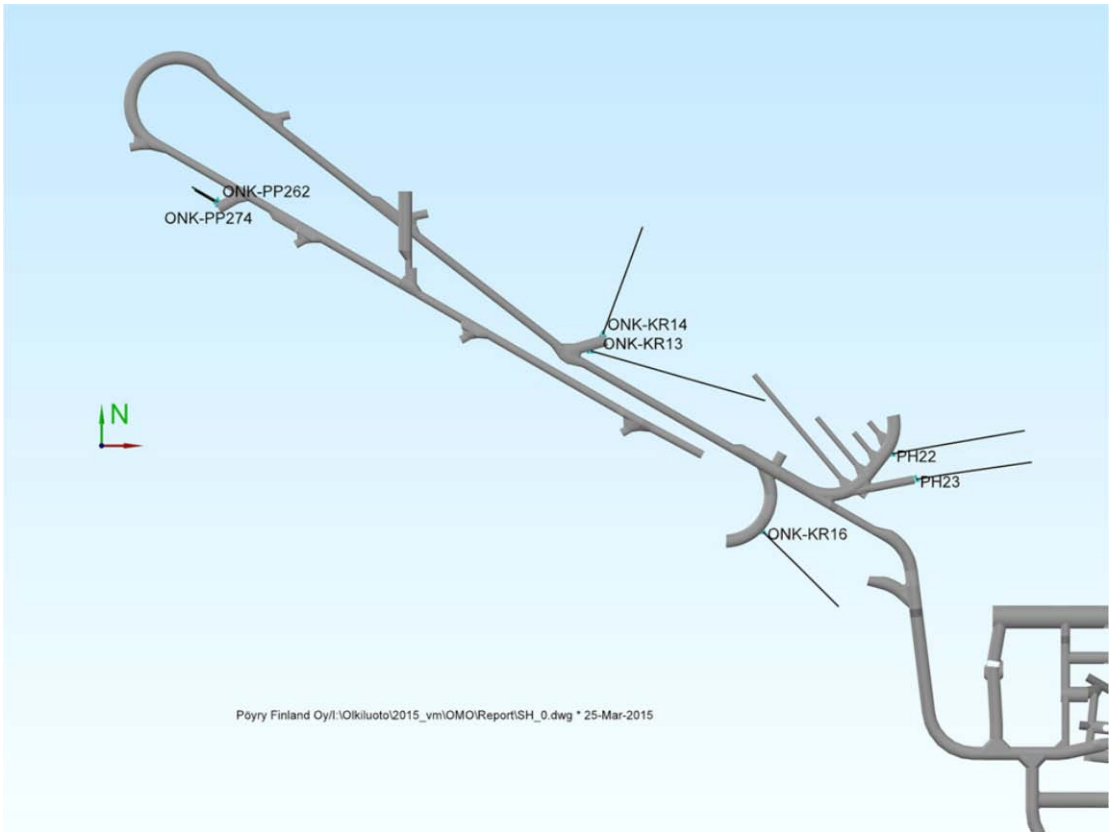

Figure 1.2. The location of packed- off drillholes in ONKALO at the end of 2014. From Vaittinen et al. (2015, Figure 3-7).

2 Background

2.1 Concepts of groundwater flow in sparsely fractured rock

Groundwater flow in sparsely fractured crystalline rock such as granite or gneiss has been described in terms of at least three alternative concepts:

- Discrete-fracture networks
- Sparse-channel networks
- Equivalent porous-medium representations

The first of these concepts, discrete-fracture networks, is most commonly envisioned as a network of plate-like, 2-D conductors (disks or rectangles) that connect to form a network in 3-D space. The aggregate behavior for flow and transport is governed by the spatial density (also referred to as intensity) of fractures, which is inversely related to the distance between connections in the network. At low densities near the percolation threshold, the network is only sparsely connected, or might only form connections over small scales. At higher densities, each fracture may connect to several other fractures to form a densely connected system.

In such a system, a well test in a drillhole section that intersects a single large, transmissive fracture would tend to exhibit behavior similar to a well test in a tabular aquifer, with the pressure disturbance and flow radiating in the plane of the fracture until arriving at intersections with other fractures, and then continuing to diverge on the network scale for the duration of the disturbance.

A sparse channel network (Black et al., 2006) considers that the flow system consists of a network of features that connect with each other only at large distances, typically larger than would result from a network formed by equidimensional (disk- or square-shaped) fractures. In such a system, a well test would show little indication of diverging flow. Even when a junction with another channel is reached, the flow system would remain essentially linear. This differs from well-connected channel systems (e.g. lattice models such as that of Moreno and Neretnieks, 1991) in which flow diverges at each node in the network.

Equivalent-porous medium representations of fractured rock are based on the concept of a representative elementary volume within which the density of fracturing and interconnections are sufficient to form a well-connected flow system that approximates the behavior of a porous medium.

2.2 Propagation of transient hydraulic disturbances

2.2.1 Conventional porous-medium models in 2D and 3D

The basic flow system geometries considered in classical well-test analysis include: linear (1-D), cylindrical (2-D), and spherical (3-D) flow systems. These integral-dimension geometries can also arise in fractured rock, as illustrated in Figure 2.1.

In fractured rock the effective flow dimension can change from one test section to the next, because it depends upon the highly variable configurations of the fractures that intersect the wellbore. The value of conductivity estimated from the final flowrate in a test can vary by as much as two orders of magnitude, depending upon the assumed flow dimension (Doe and Geier, 1990). Therefore, when analyzing well tests in fractured rock, it is important to use a model of appropriate dimension.

2.2.2 Generalized radial flow model

The generalized radial flow (GRF) methodology is based upon a generalization, introduced by Barker (1988), of the concept of flow dimension in a well test. The concept of generalized flow dimension is most easily understood as an extension of the basic flow system geometries considered in classical well test analysis.

As noted by Barker (1988), in fractured rock

the dimension of the flow system is generally not known a priori. There is little reason to assume that the flow system will behave in accordance with any of these simple geometries. Flow system geometries intermediate to the integral dimension cases, referred to as fractional dimension cases, can also be envisioned.

The generalized radial flow model developed by Barker (1988) on this idea of treating flow dimension as a continuous rather than discrete variable. The model is based on the following main assumptions:

- Flow obeys Darcy's law.
- Radial, n-dimensional flow emanates from a single source into a space-filling, homogeneous and isotropic conduit.
- The source is an n-dimensional sphere (e.g. a cylinder for 2-D flow or a sphere for 3-D flow) of radius r_w, and storage capacity S_w defined as the volumetric change in wellbore storage per unit change in head.

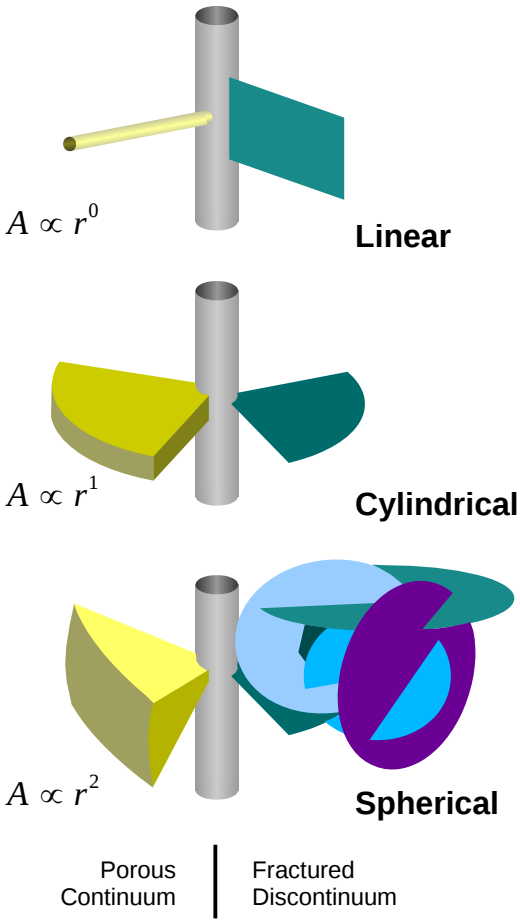

Figure 2.1. Conceptual illustration how 1-D, 2-D, or 3-D radial flow can arise in either porous media or fractured rock, depending on how the conductive cross-sectional area A of an aquifer/conduit or fracture network varies with distance r from the wellbore.

The term space-filling above means that the conduit entirely fills the n-dimensional space. For example, in a 2-D aquifer the flow occurs radially in all directions in the plane of the aquifer. The assumption of a space-filling conduit, can be relaxed as discussed below. Barker's GRF model also included an infinitesimal skin around the source. However, in the present study no skin is assumed, and the equations presented below have been reduced to the case of zero skin.

The GRF equations are developed in terms of a system of n-dimensional, concentric spherical surfaces. The area of these surfaces varies with distance r from the center as:

$$A_c = \alpha_n r^{n-1}$$

and α_n is an n-dimensional angle defined by:

$$\alpha_n = \frac{2\pi^{n/2}}{\Gamma(n/2)}$$

and $\Gamma(z)$ is the gamma function of argument z. For the integral dimension cases, this n-dimensional angle takes values of $\alpha_1 = 2$, $\alpha_2 = 2\pi$, and $\alpha_3 = 4\pi$.

As can be seen from the 2-D case, α_n is a space-filling angle. Conduits that are less than space-filling may be accounted for by multiplying α_n by a factor $\theta/2\pi$, equal to the fraction of the n-dimensional space that is filled by the conduit (Doe and Geier, 1990). The characteristic flow behavior for a particular dimension, n, will be observed in any system, space-filling or not, for which the conducting surface area A_n varies with distance r along the conduit in proportion to r^n-1.

Using the relationships above, Barker (1988) developed a generalized radial flow equation for the case where hydraulic conductivity K is uniform within a given conduit:

$$\frac{K}{r^{n-1}}\frac{\partial}{\partial r}\left(r^{n-1}\frac{\partial h}{\partial r}\right) - S_s\frac{\partial h}{\partial t} = 0$$

where:

h	= hydraulic head	[L]
K	= hydraulic conductivity of the conduit	[LT^{-1}]
S_s	= specific storage of the conduit	[T^{-1}]

As pointed out by Doe and Geier (1990), the effective flow dimension can also be interpreted in terms of the rate at which the product of cross-sectional area and hydraulic conductivity ($A_c \cdot K$) increases with distance from the wellbore. Examples of equivalent cases for integral dimensions n = 1, 2, and 3 are illustrated in Figure 2.2.

The generalized radial-flow formulation of Barker (1988) allows consideration of cases where the effective flow dimension is intermediate to the integral-dimension cases (linear, cylindrical, or spherical) that are commonly considered. As illustrated in Figure 2.3, the possibilities are not necessarily limited to the range from linear (n = 1) to spherical (n = 3). The circumstances giving rise to sub-linear (n < 1) or hyperspherical (n > 3) flow cannot persist indefinitely, but can occur over the limited scale of a well test.

From the generalized radial-flow equation as given above, solutions for specific types of situations arising in well test interpretation have been developed (Barker, 1988; Doe and Geier, 1990). These can be used to compare with observed changes in heads and flowrates, as detailed in Appendix 1. Key results are summarized below.

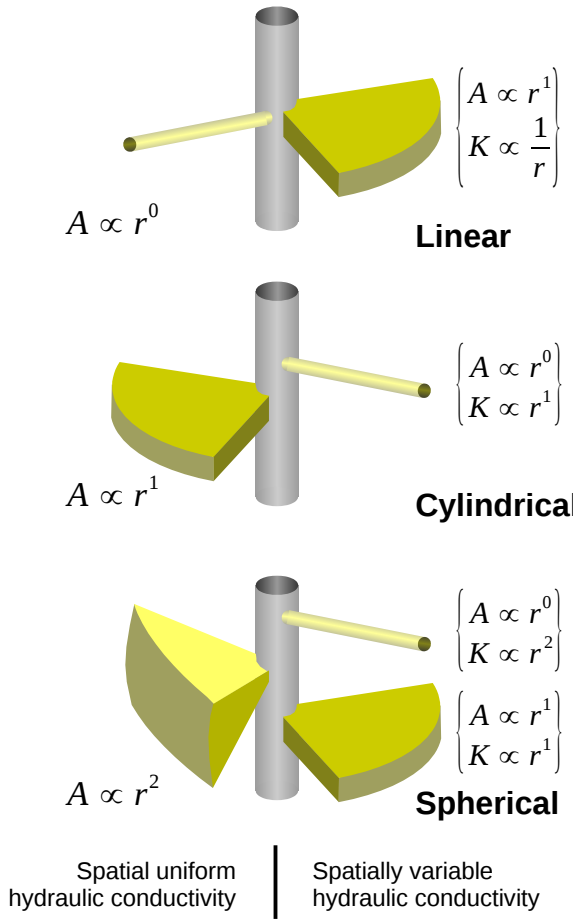

Figure 2.2. Conceptual illustration of how apparently 1-D, 2-D, or 3-D radial flow can arise in porous media depending on how either the conductive cross-sectional area *A* of an aquifer/conduit, or the product *KA*, varies with distance *r* from the wellbore.

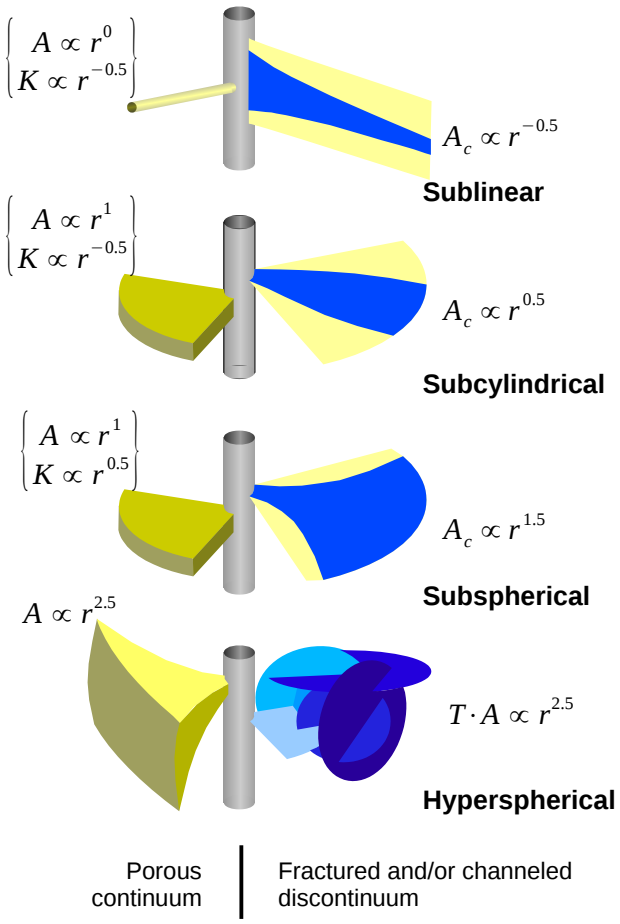

Figure 2.3. Conceptual illustration of how sub-linear, hyperspherical, or non-integral dimension flow can arise in porous media depending on how either the conductive cross-sectional area *A* of an aquifer/conduit, or the product *KA*, varies with distance *r* from the wellbore.

Table 2.1. Head h as a function of distance r and time t for special cases of integral-dimension flow.

Type of flow	Flow dimension n	$h(r,t)$
Linear	1	$\frac{Q_o r}{2\sqrt{\pi}Kb^2}\left(\frac{e^{-u}}{\sqrt{u}}-\sqrt{\pi}\,\mathrm{erfc}\sqrt{u}\right)$ [1]
Cylindrical	2	$\frac{Q_o}{4\pi Kb}W(u)$ [2]
Spherical	3	$\frac{Q_o}{4\neq Kr}\mathrm{erfc}\sqrt{u}$ [1]

[1] erfc(u) is the complementary error function.

[2] W(u) is the well function of Theis (1935), also known as the exponential integral function.

Constant-rate pumping test: Infinitesimal well

For a pumping test in which a section of length b in a pumping well of radius r_w is pumped at a constant rate Q_o, for the bounding case of an infinitesimal well (i.e. r_w approaching 0), Barker (1988) obtained a closed-form solution:

$$h(r,t)=\frac{Q_o r^{2\nu}}{4\pi^{1-\nu}Kb^{3-n}}\Gamma\left(-\nu,\frac{r^2}{4\eta t}\right)$$

where:

$\nu = 1 - n/2$

$$u=\frac{r^2 S_s}{4Kt}$$

and $\Gamma(\nu,u)$ is the incomplete gamma function (Abramowitz and Stegun, 1964). Special cases of integral-dimension flow are summarized in Table 2.1 for comparison to standard well-test formulas.

Thus the function $\Gamma(1\text{-}n/2,u)$ can be viewed as a generalized well function. Values of this function for flow dimension n ranging from 1 to 3 are shown in Figure 2.4. Type curves of this form can be matched to drawdown data either graphically or numerically to obtain best estimates of the flow dimension and hydraulic diffusivity.

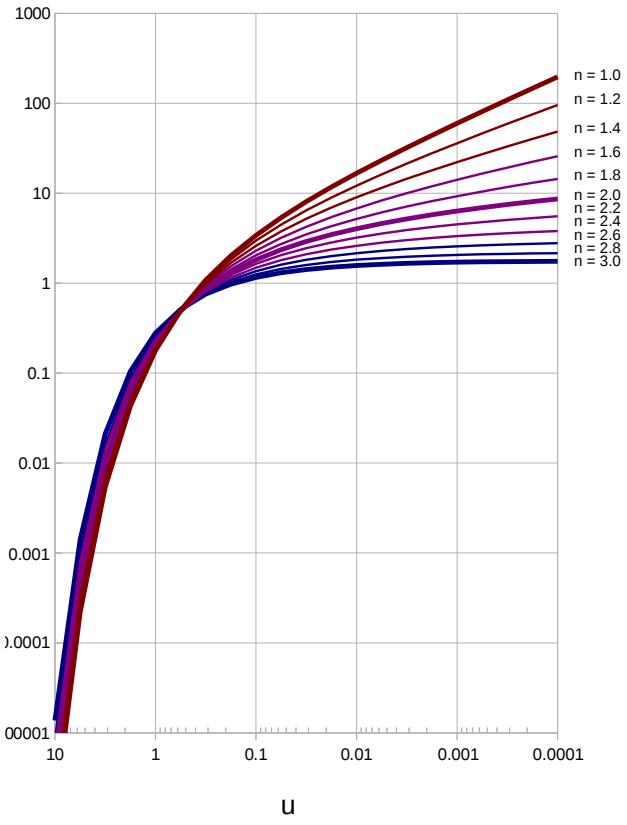

Figure 2.4. Generalized well function $\Gamma(1\text{-}n/2,u)$ for flow dimensions n ranging from 1 to 3 (according to the legend).

Constant-rate pumping test: Finite-diameter well

For a finite-diameter well a Laplace transform solution is available (Barker, 1988; Ball et al., 1991):

$$\bar{h}(r,s) = \frac{Q_o r^{\nu} r_w^{\ \nu} K_{\nu}\left(r\sqrt{\frac{s}{\eta}}\right)}{sKb^{3-n}\alpha_n \lambda K_{\nu-1}\left(r_w\sqrt{\frac{s}{\eta}}\right)}$$

but no closed-form solution is available. Therefore calculation of values of the function $h(r,t)$ requires numerical inversion of the Laplace-transform solution.

Constant-pressure injection test

Laplace-space solutions for the case of constant-pressure (or constant-head) injection tests were developed by Doe and Geier (1990) based on the general solution of Barker (1988). For the case of negligible skin effect and constant head h_{wo} applied at the wellbore, the Laplace transform of flow rate into the rock is:

$$\bar{Q}(s) = h_{wo} K b^{3-n} \alpha_n r_w^{n-2} \frac{1}{s} \Phi\left(r_w\sqrt{\frac{sS_s}{K}}\right)$$

where the function $\Phi_{\nu}(z)$ is defined as:

$$\Phi_{\nu}(z) = \frac{zK_{\nu-1}(z)}{K_{\nu}(z)}$$

Calculation of values of the corresponding function $Q(t)$ requires numerical inversion of the Laplace-transform solution, as for the preceding case.

3 Available data and previous analyses

3.1 Monitoring of hydraulic head or pressure in drillholes

Hydraulic head and pressure monitoring data were provided on in digital format by Posiva for open, multi-packered, and packed-off drillholes. These data included:

Water levels in open OL-KR drillholes corresponding to plots in:

- Appendix 9 of Vaittinen et al. (2013)
- Appendix 9 of Vaittinen et al. (2014)
- Appendix 9 of Vaittinen et al. (2015).

Heads in multi-packered OL-KR drillholes corresponding to plots in:

- Appendix 10 of Vaittinen et al. (2013)
- Appendix 10 of Vaittinen et al. (2014)
- Appendix 10 of Vaittinen et al. (2015).

Drawdowns in packed-off OL-KR drillholes corresponding to plots in:

- Appendix 11 of Vaittinen et al. (2014)
- Appendix 11 of Vaittinen et al. (2015).

Digital versions of groundwater pressures in packed-off ONKALO drillholes corresponding to plots in:

- Appendix 12 of Vaittinen et al. (2014)
- Appendix 12 of Vaittinen et al. (2015).

Supplementary data included corrections for surficial fluctuations, earth tides, and atmospheric pressure, including: Time series for the reference groundwater level fluctuation during 2001–2014, and earth tide and atmospheric pressure correction time series coefficients for 2001–2014.

In order to permit evaluation of excavation effects in ONKALO, the time schedule for advancement of the ONKALO facility was provided as a time series giving the chainage for excavation face of main ONKALO access ramp as a function of calendar date.

3.2 Cross-hole hydraulic interference tests

Data were also provided for cross-hole/interference tests at Olkiluoto including:

- Hydraulic cross-hole tests in OL-KR14 – OL-KR18
- Hydraulic cross-hole tests during long-term pumping in OL-KR24
- Detailed interference (cross-hole) tests between boreholes ONK-PP262 and ONK-PP274.

4 Methods

4.1 Selection and preliminary processing of data

An initial step in the analysis is to identify monitoring intervals that are more likely to reflect the response of the sparsely fractured rock rather than the response of the hydrogeological zones.

Intersections of hydrogeological zones with drillholes were compiled from tables given by Vaittinen et al. (2011), as listed in Appendix 2. This compilation includes both confirmed hydrogeological zones that were included in the hydrogeological site model, as well as "possible" hydrogeological zones that were assessed as being either "high confidence" or "medium confidence."

From this information, for each drillhole (or drillhole section) in which a hydraulic disturbance was induced, the observation drillholes/sections were identified that are connected directly via a hydrogeological zone. The responses observed in the remaining sections can be interpreted as more likely to be representative of the sparsely-fractured rock.

4.2 Corrections for surficial effects

The reference water table fluctuation as evaluated by Vaittinen et al. (2015) for the period from January 1, 2001 through December 31, 2015 is plotted in Figure 4.1. The general tendency is for an annual cycle in which the water table rises with the onset of snow melt in spring, and then decline in fall, but shorter-term fluctuations are also apparent.

For analysis of drawdowns in response to excavation and other disturbances, the reference water table fluctuation is subtracted from the head monitoring data.

Vaittinen et al. (2015) describe further corrections for earth tide effects and atmospheric pressure effects. The earth tide effects have a peak-to-peak amplitude generally less than 10 cm with nominally two cycles per day. Corrections for these effects can be made using TSoft (Van Camp and Vauterin, 2005), using coefficients calculated using the same software by Vaittinen et al. (2015). These coefficients were provided as part of Posiva's data delivery for

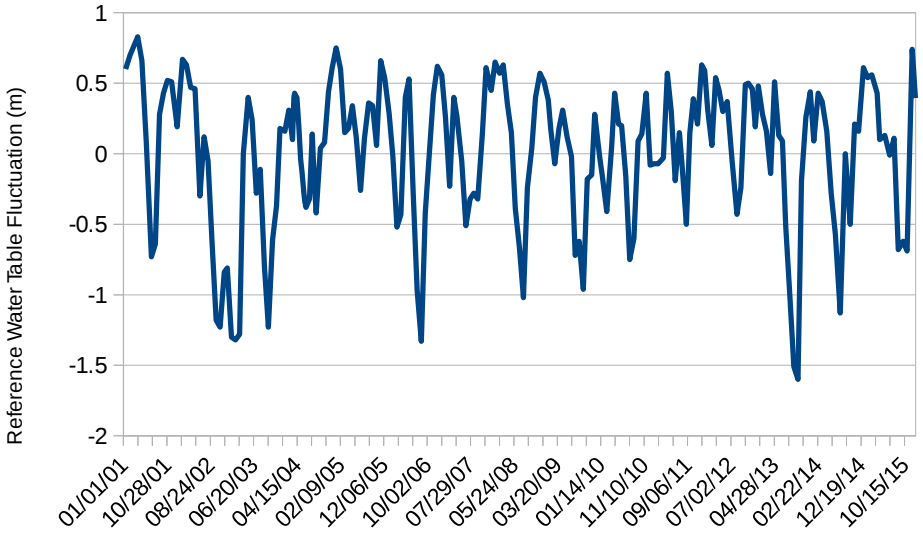

Figure 4.1 Reference groundwater level 2001–2015.

the present analysis, but implementation in the TSoft program was found to be a more complex process than anticipated. Hence these corrections have not been applied for the analyses presented here.

4.3 Diagnostic plots and methods of interpretation

Graphical analysis

A graphical method for diagnosis of generalized radial flow in response to large-scale cross-hole tests was suggested by Ball et al. (1991) based on classical methods of type-curve analysis. The steps in the method are:

1. Plot drawdown $h_o - h$ vs. the time divided by distance squared (t/r^2) for data from multiple observation drillholes or sections, on a logarithmic scale;
2. Identify clusters of observation drillholes/sections that show similar response characteristics on this type of plot, and
3. For each of these groups, fit the data to the generalized radial-flow type curves, i.e. the generalized well function $\Gamma(1\text{-}n/2,u)$ as plotted in Figure 2.4.

Clusters of similarly responding observation sections can indicate that a particular hydrogeological zone controls propagation of the hydraulic disturbance to these sections. The flow dimension for each such cluster can be estimated from the type curve that provides the best match (by eye or by a more mathematically rigorous criterion). Deviations of individual observation sections may provide further insight into the heterogeneous response either within the controlling structure, or indirect connections via the sparsely-fractured rock.

For pumping tests, the distance r between the pumping interval and the observation interval was calculated as the distance between the midpoints of the two intervals:

$$r = \left\| \frac{x_{p,top} + x_{p,bot}}{2} - \frac{x_{o,top} + x_{o,bot}}{2} \right\|$$

where $x_{p,top}$ and $x_{p,bot}$ are respectively the coordinates of the top and bottom of the pumped interval, and $x_{o,top}$ and $x_{o,bot}$ are respectively the coordinates of the top and bottom of the observation interval. It may be noted that this does not necessarily represent the shortest distance between each pair of intervals, nor the shortest "hydraulic" distance as this might be measured within the plane of a hydrogeological zone that intersects both features.

Numerical analysis

More quantitatively rigorous results can be obtained by an automated curve-fitting procedure.

In the present analysis this has been done for pumping test data based on the Laplace-transform solution for a finite-diameter well as given in Section 2. Numerical inversion of the Laplace-transform solution is accomplished by means of the algorithm of Stehfest (1970).

Automated curve-fitting is accomplished by means of the downhill simplex method (Nelder and Mead, 1965; Press et al., 1986), to minimize the mean square error in observed vs. modeled drawdowns, weighted inversely by the time t from the start of the pumping test:

$$F(n,K,S_s) = \sum_i \frac{\left[h_{obs}(t_i) - h_{model}(t_i;n,K,S_s)\right]^2}{(t_i - t_o) + \delta_t}$$

where:

t_i = time of the ith data point [T]
t_o = starting time of the disturbance [T]
δ_t = nominal small increment of time [T]
$h_{obs}(t_i)$ = head value observed at time t_i [L]
$h_{model}(t_i; n, K, S_s)$ = head value predicted by the model at time t_i for a given n, K and S_s [L]

The inverse weighting with respect to t is aimed to emphasize the early-time points which are very few in number relative to the late-time points, but can represent the most distinctive part of the response. For the present evaluations a value of $\delta_t = 0.1$ s was used.

The search algorithm was applied successively to optimize K and S_s for each value of n in the range 0.5 to 3.5, on increments of 0.1 (i.e., n = 0.5, 0.6, …, 3.5), and then the triplet of (n, K, S_s) values of that yielded the minimum value of $F(n, K, S_s)$ was chosen as the global optimum. As discussed in section 2.2.2, the circumstances giving rise to sub-linear ($n < 1$) or hyperspherical ($n > 3$) flow cannot persist indefinitely, but can occur over the limited scale of a well test.

5 Results

5.1 Resolution of data from monitoring of heads in drillholes

Monitoring of heads in drillholes has been carried out by a combination of automated and manual measurements (Vaittinen et al., 2014; Vaittinen et al., 2015). The median time interval between measurements varied depending on the dataset:

- Manual measurements of water levels in open drillholes: Median interval generally about one week, except KR06 (1 day), KR42 (9 days), KR26 (10 days), and KR30 and KR53 (14 days).
- Automatic registration of head measurements in packed-off KR holes: Median interval generally 1 hour, except KR08 and KR27 (15 minutes).
- Automatic registration of head measurements in drillholes in ONKALO: Median interval generally 15 minutes except ONK-PP26 and ONK-PP27 (10 seconds).

These intervals between measurements limit the potential to interpret transient responses to quasi-steady perturbations, particularly for cases where the starting point of the disturbance is not known with any greater precision. A perturbation would need to persist at least 3 years to provide observations spanning two orders of magnitude on the time scale, for the manual measurements, or 40 days for the automatic measurements in most surface-based drillholes. The more frequent measurements in KR08, KR27, and most drillholes in ONKALO would still require perturbations lasting 10 days, to provide data spanning three orders of magnitude in time.

The much more frequent measurements in ONK-PP26 and ONK-PP27, on nominally 10 second intervals, could allow analysis of more brief perturbations with durations as brief as a few hours. However these drillholes have already been used for a generalized radial-flow analysis of responses to cross-hole responses on a detailed scale by Hansson et al. (2014), as discussed below. Thus it was judged that an analysis of responses to less well-characterized perturbations would yield little additional information.

5.2 Interpretations of cross-hole interference tests

Long-term pumping test in OL-KR24

Intersections of hydrogeological zones with the drillhole intervals monitored in long-term pumping test in OL-KR24 are listed in Table 5.1. Most of the observation intervals are connected directly to the pumping well via one or more hydrogeological zones. In particular, HZ19A is responsible for many direct connections.

Applying the graphical method for large-scale cross-hole tests, a preliminary plot of drawdown $h_o - h$ vs. the time divided by distance squared (t/r^2) yields the result shown in Figure 5.1.

A cluster of similarly responding observation intervals is readily from this plot, namely: OL-KR4, OL-KR7, OL-KR8, OL-KR10, OL-KR14, OL-KR15B, OL-KR16B, OL-KR18B, OL-KR22, OL-KR28. From Table 5.1 it can be noted that all of these have direct connections to the pumping well via HZ19A. For brevity these intervals will be referred to here as “Cluster 1.”

A type curve for 2-D flow ($n = 2$) provides a reasonable match to the aggregate behavior for Cluster 1, as shown in Figure 5.2. The most noticeable deviation from infinite-acting cylindrical flow is in OL-KR28, which displays a more complex response in late time (possibly related to network effects in the site-scale network of hydrogeological zones, which is outside the scope of the present analysis focusing on the sparsely fractured rock).

Excluding the data from Cluster 1, the responses

Table 5.1. Intersections of hydrogeological zones with drillholes monitored in long-term pumping test in OL-KR24.

Hydrogeological Zone	Drillhole intersected	Top (m)	Bottom (m)
BFZ100	OL-KR22	337.7	340.5
	OL-KR23	372.5	373
	OL-KR25	216.5	222.1
	OL-KR26	95.8	98.3
	OL-KR28	177.02	178.02
	OL-PH01	151.6	154.3
BFZ161	OL-KR04	808.3	809.95
HZ146	OL-KR27B	9.3	11.3
HZ19A	OL-KR04	80.5	84.1
	OL-KR08	80.6	83.3
	OL-KR10	39.8	41.8
	OL-KR14	50	52
	OL-KR15B	19.1	25.1
	OL-KR16B	17	19
	OL-KR17B	8	10
	OL-KR18B	31.3	33.3
	OL-KR22	96.1	102.7
	OL-KR23	88.7	94.7
	OL-KR24	93	95.3
	OL-KR25	58.6	64.6
	OL-KR27	129	133
	OL-KR28	134	140
HZ19B	OL-KR04	140.6	142.6
	OL-KR07	46.9	48.8
	OL-KR08	249.1	255.9
	OL-KR22	146.9	152.7
	OL-KR23	192.8	197
	OL-KR24	114.5	116.8
	OL-KR25	123.3	125.3
	OL-KR27	256.8	262.7
	OL-KR28	170	180.2
HZ19C	OL-KR04	115	117.8
	OL-KR08	106	114.8
	OL-KR10	60.6	64.8
	OL-KR14	79	81
	OL-KR22	108.3	113.2
	OL-KR23	135.2	137.2
	OL-KR24	114.5	116.8
	OL-KR25	94.6	97.5
	OL-KR27	207	211
	OL-KR28	155.4	159.4

Hydrogeological Zone	Drillhole intersected	Top (m)	Bottom (m)
HZ20A	OL-KR04	306.2	314.9
	OL-KR07	224.2	249.9
	OL-KR08	451.7	454.5
	OL-KR10	260	262
	OL-KR22	390.4	392.4
	OL-KR23	425.9	430
	OL-KR24	303.6	306
	OL-KR25	342.6	352.5
	OL-KR27	503.8	505.8
	OL-KR28	388.3	390.8
HZ20B	OL-KR04	365.3	367.3
	OL-KR07	279.6	287.1
	OL-KR08	547.6	561
	OL-KR10	326.6	328.6
	OL-KR22	423	426.4
	OL-KR24	396	398.3
	OL-KR25	405.5	408.8
	OL-KR28	442.9	447.2
HZ21	OL-KR04	756.8	764.2
	OL-KR07	689.5	711.6
HZ21B	OL-KR04	862.9	864.9
none	OL-KR22B	–	–
	OL-KR23B	–	–
	OL-KR25B	–	–
	OL-KR28B	–	–

in the remaining observation intervals can be discussed in terms of the following clusters or groups (using the term "cluster" for intervals that are clustered on the plot of drawdown vs. normalized time t/r^2, and "group" for intervals that are not clustered but show similar qualitatively patterns of response):

Group 2: Intervals with early cylindrical behavior but late-time disturbance

OL-KR22B, shows early-time cylindrical behavior similar to Cluster 1 but then the drawdown decreases abruptly by about a factor of two, about 26 days into the pumping test. The upper (T1) interval in OL-K23B shows a similarly abrupt decrease in drawdown at the same time (though farther to the right on this plot due to the effect of scaling by the distance squared).

The early-time response in both of these intervals can be approximated reasonably well by 2-D type curves (Figure 5.3). These deviations in later time apparently represent a disturbance in the vicinity of these two shallow drillhole intervals.

Cluster 3: Intervals with early cylindrical behavior but apparent late-time decrease in flow dimension

The two intervals in OL-KR25B show nearly identical responses. As seen in Figure 5.4 the early-time parts of these two curves can be matched approximately by a 2-D type curve. The increasing slope in late time, however indicates a departure from any simple radial-flow model. This could be interpreted as a boundary effect (a "hydraulic choke") or a transition to a lower-dimensional flow system with distance from the source, via the part of the fracture system that connects to these observation intervals.

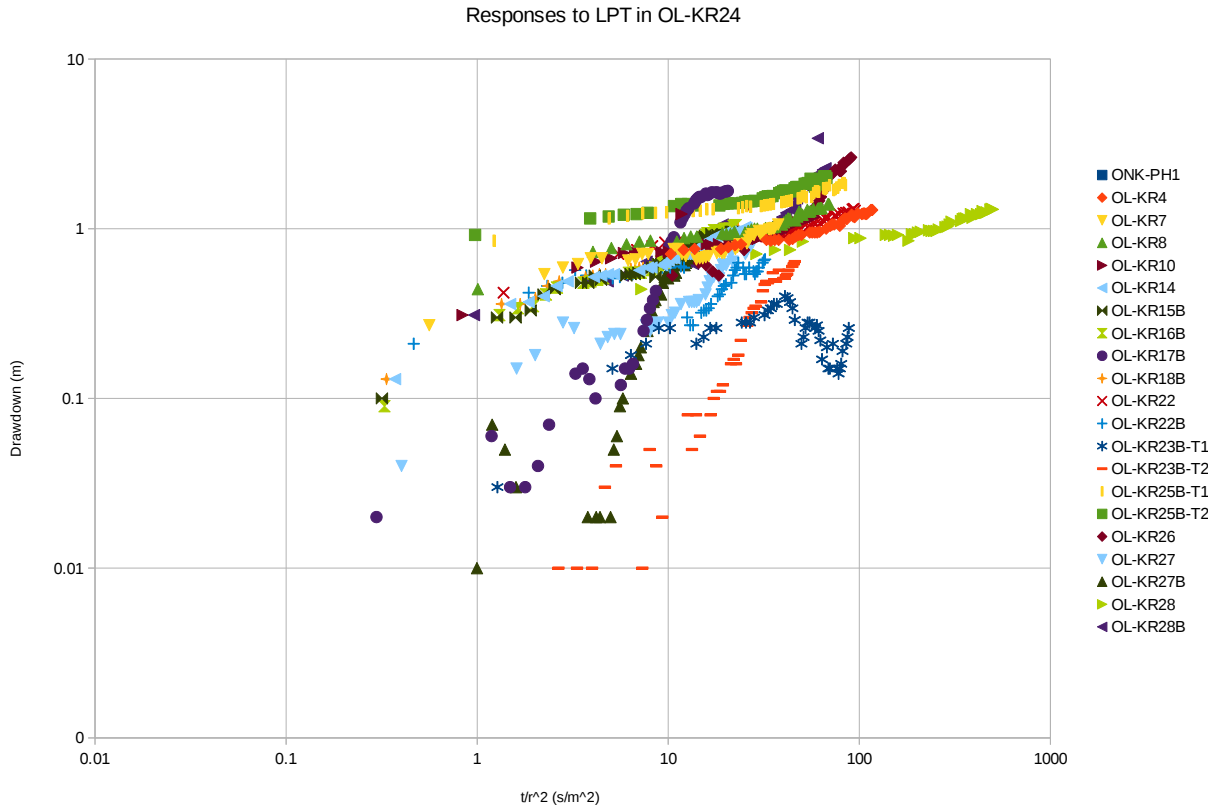

Figure 5.1. Time/distance-drawdown plot of all measured drawdowns in response to the long-term pumping test in OL-KR24.

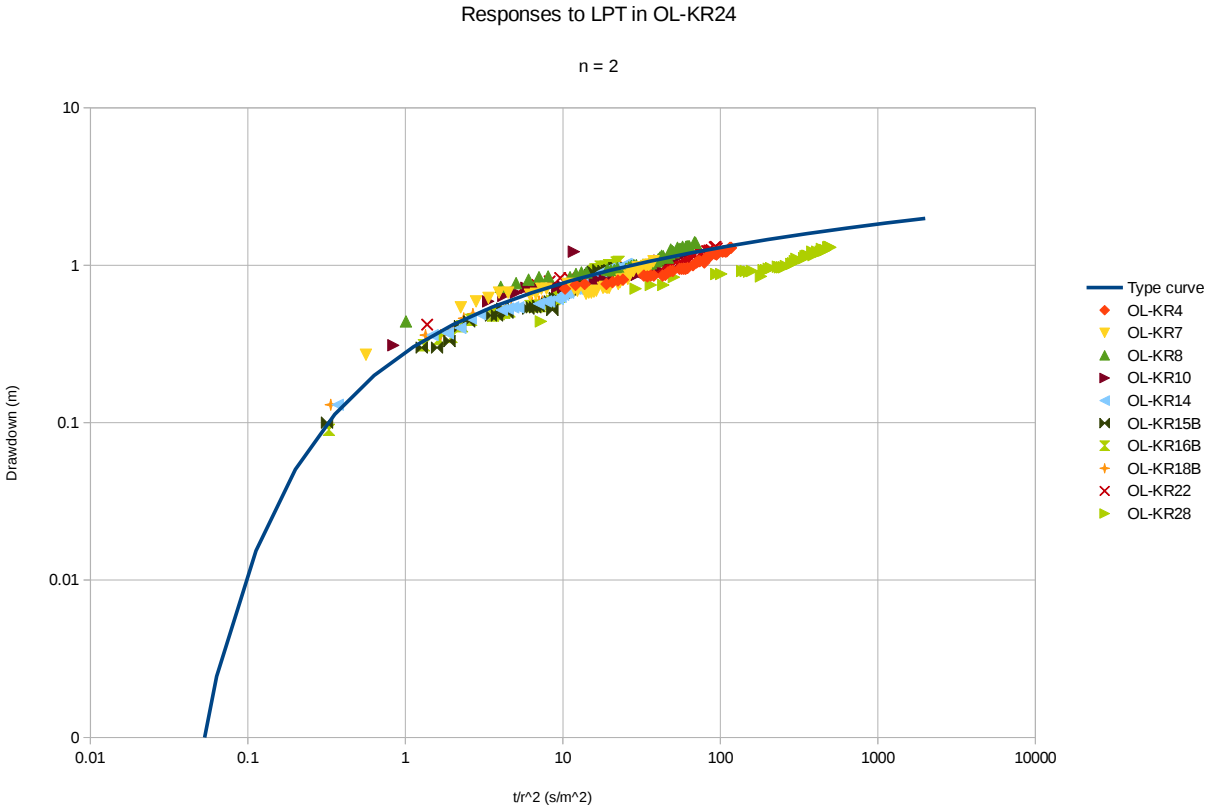

Figure 5.2. Time/distance-drawdown plot of Cluster 1 observation intervals showing similar responses to the long-term pumping test in OL-KR24, with match to type curve for cylindrical flow ($n = 2$).

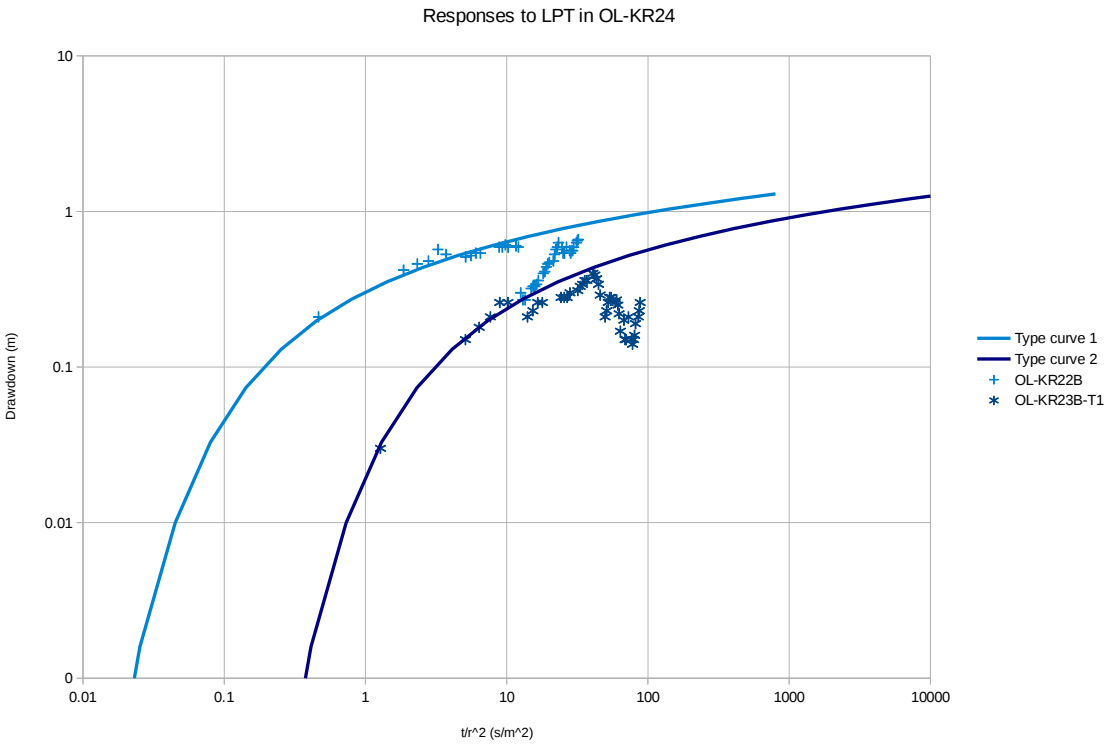

Figure 5.3. Time/distance-drawdown plot of Group 2 observation intervals showing early cylindrical flow responses to the long-term pumping test in OL-KR24 but late-time disturbances. The two type curves show manual matches for cylindrical flow ($n = 2$).

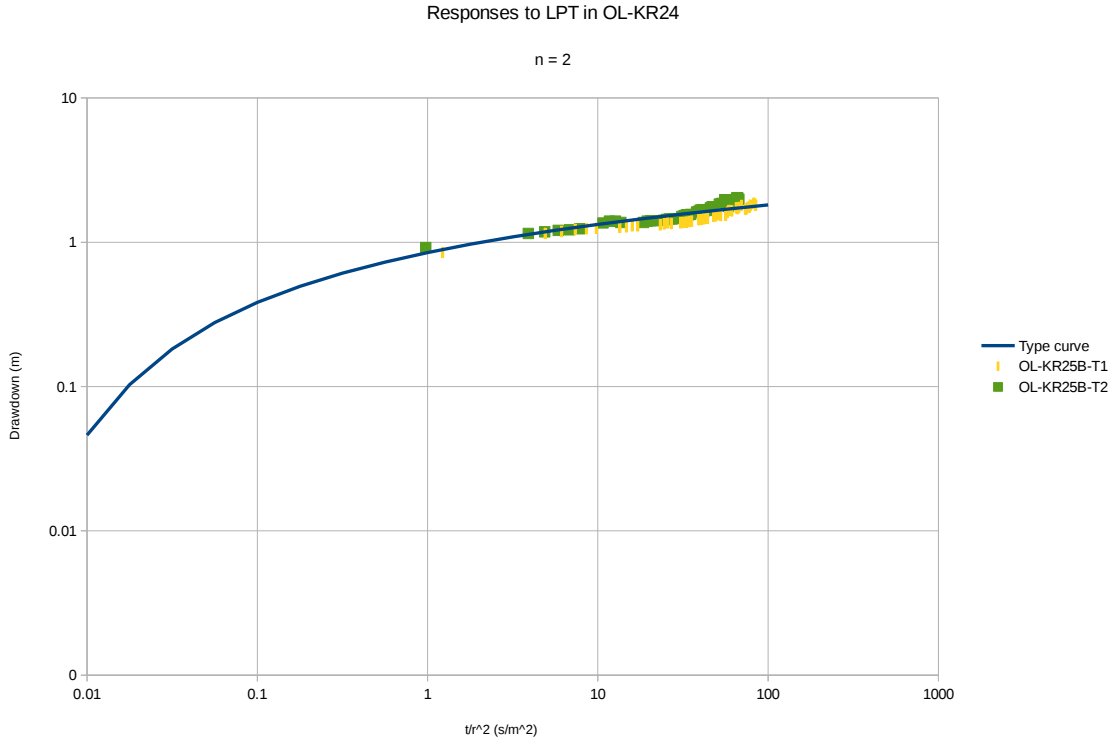

Figure 5.4. Time/distance-drawdown plot of measured drawdowns in response to the long-term pumping test in OL-KR24, in the two observation intervals in OL-KR-25B (Cluster 3).

Cluster 4: Intervals with sub-cylindrical behavior but late-time deviation

Three observation drillholes (OL-KR26, OL-KR27, and OL-KR28B) form a loose cluster on the plot of drawdowns vs. normalized time (Figure 5.5), with apparently sub-cylindrical flow ($n < 2$) but late-time deviation. The general pattern of the deviation – a flattening of the response followed by a steepening, then a return to near-cylindrical behavior – is similar for the three tests. It occurs at different positions in terms of normalized time, but at similar actual times for both OL-KR27 and OL-KR28B (both of which are close to the pumped well OL-KR24) though at a later time for OL-KR26 (which is at a greater distance in the same NNE direction).

One possible interpretation is that the flow network connecting toward the NNE consists of segments with distinct effective flow dimensions. However the non-monotonic form of the data for OL-KR26 and OL-KR27 suggests that at least part of the effect could be a consequence of disturbance.

Group 5: Intervals with high flow dimension but early-time deviations

Three observation intervals (OL-KR17B, OL-KR23B-T2, and OL-KR27) show indications of high-dimensional flow in mid- to late time, but with scattered early-time data (Figure 5.6). The early time variations of hydraulic head are irregular and mainly on the scale of centimeters, so could reflect localized disturbances (and perhaps to some degree, measurement errors). In one case (OL-KR17B) there is a late-time flattening which could result from a connection of a constant-head boundary, such as a high-transmissivity hydrogeological zone connecting to the sea.

Results of automated curve-fitting

Automated curve-fitting according to the methods described above yields estimates of flow dimension and ancillary parameters as listed in Table 5.2.

The results are plotted in Figure 5.7 in terms of the cumulative distributions of flow dimensions for observation intervals with direct connections to the pumped well, vs. observation well without direct connections. The main difference that can be seen is that the flow dimensions for observation intervals with direct connections (mainly via HZ19A) are close to cylindrical or 2-D flow, while observation intervals without such direct connections tend to exhibit higher flow dimensions. The model fits to individual tests are plotted in Appendix 3.

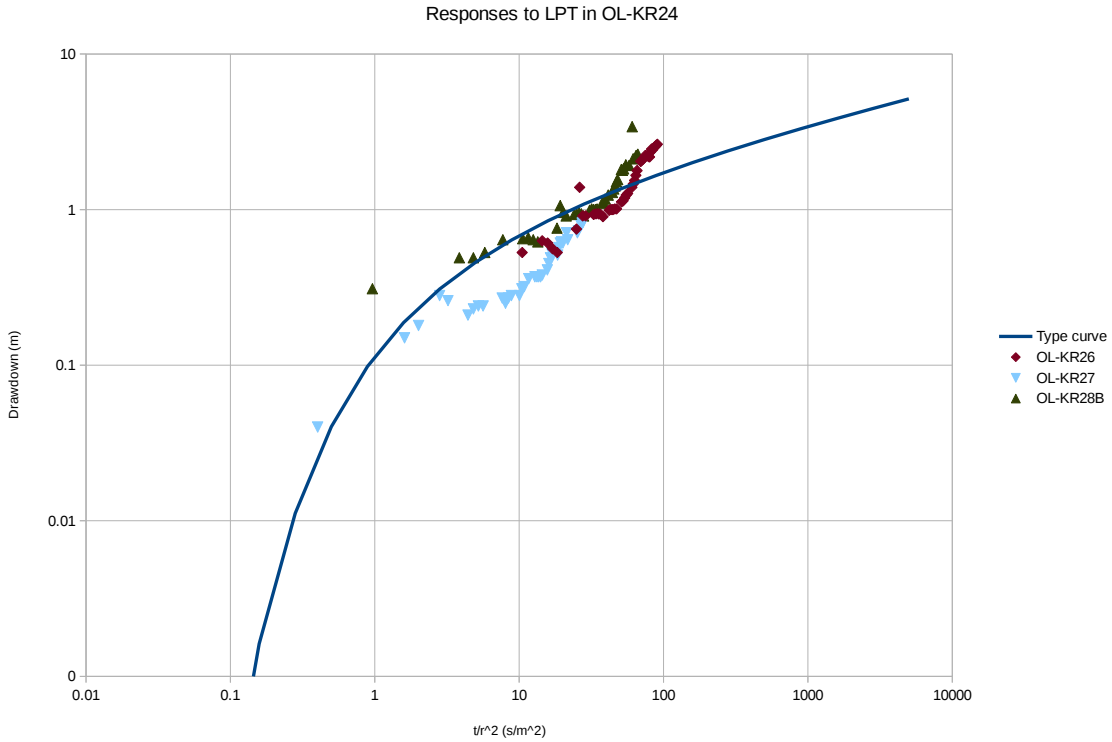

Figure 5.5. Time/distance-drawdown plot of measured drawdown responses to the long-term pumping test in OL-KR24, in observation intervals belonging to Cluster 4. A manual fit to the generalized radial-flow type curve for $n = 1.6$ is shown for comparison.

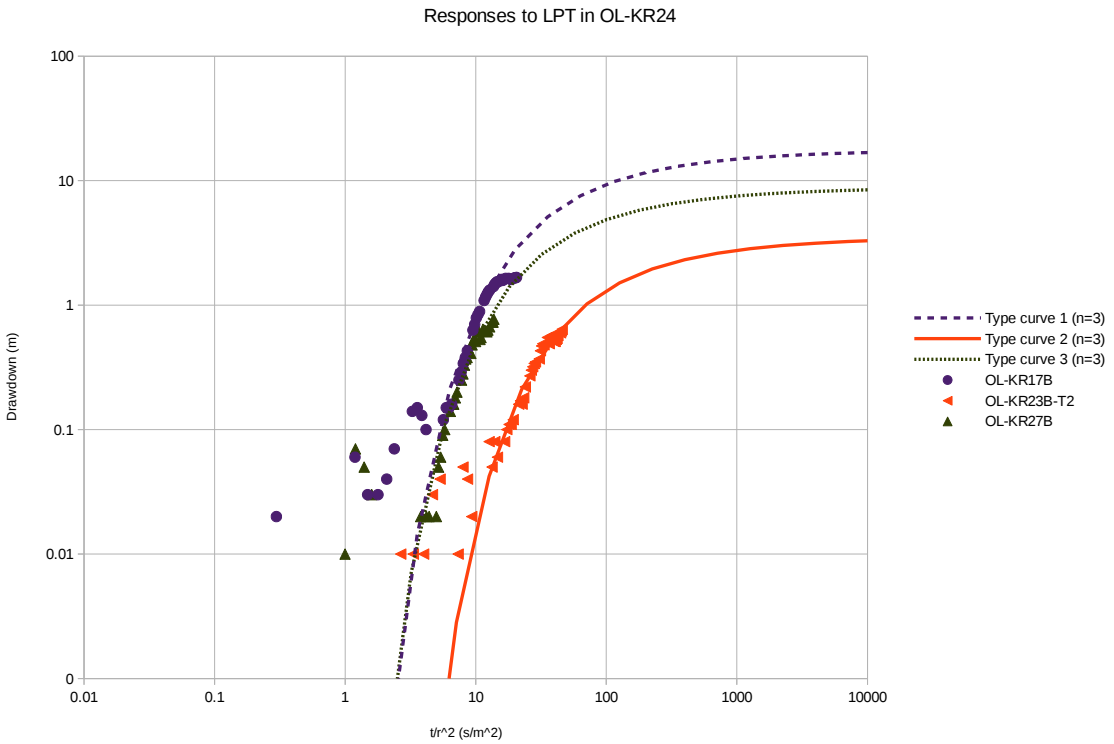

Figure 5.6. Time/distance-drawdown plot of measured drawdown responses to the long-term pumping test in OL-KR24, in observation intervals belonging to Group 5. Manual fits to the generalized radial-flow type curve for $n = 3$ (spherical flow) are shown for each case.

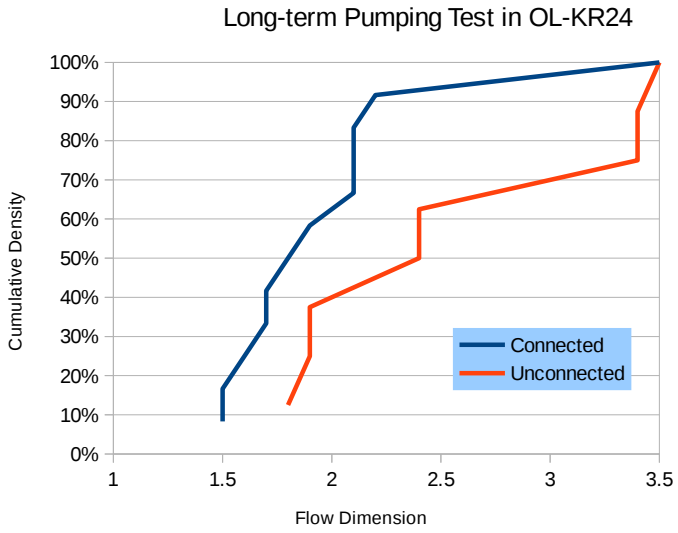

Figure 5.7. Cumulative distributions of flow dimensions estimated from responses to the long-term pumping test in OL-KR24.

Table 5.2. Results of automated curve-fitting of a generalized radial-flow model to responses to the long-term pumping test in OL-KR24.

Monitoring drillhole or drillhole section	Cluster or Group	Flow Dimension *n*	Hydraulic Conductivity *K* (m/s)	Specific storage S_s (1/m)
OL-KR15B	1	1.5	1.53E-005	3.68E-006
OL-KR16B	1	1.5	1.38E-005	3.89E-006
OL-KR14	1	1.6	1.10E-005	1.59E-006
OL-KR18B	1	1.7	5.44E-006	1.80E-006
OL-KR4	1	1.7	8.33E-006	3.42E-007
OL-KR26	4	1.8	4.55E-007	1.36E-005
OL-KR27	4	1.8	4.04E-006	4.89E-006
OL-KR25B-T1	3	1.9	2.63E-006	3.15E-008
OL-KR28	1	1.9	2.32E-006	2.21E-006
OL-KR28B	4	1.9	9.29E-007	3.34E-006
OL-KR10	1	2.1	9.66E-007	3.26E-007
OL-KR22	1	2.1	9.51E-007	3.57E-007
OL-KR8	1	2.1	9.14E-007	2.95E-007
OL-KR7	1	2.2	7.26E-007	1.88E-007
OL-KR23B-T2	5	2.4	5.81E-008	7.30E-006
OL-KR25B-T2	3	2.4	2.06E-007	8.39E-008
OL-KR22B	2	3.4	1.31E-008	1.16E-008
OL-KR23B-T1	2	3.4	4.49E-008	3.55E-007
OL-KR17B	5	3.5	6.44E-010	4.32E-008
OL-KR27B	5	3.5	8.41E-010	4.92E-008

Interpretations of medium-scale pumping tests in OL-KR14 through OL-KR18

Intersections of hydrogeological zones with the drillhole intervals monitored in long-term pumping test in OL-KR14 through OLKR18 are listed in Table 5.3. OL-KR10, OL-KR14, OL-KR15, OL-KR16, OL-KR17, OL-KR18 are all directly connected by hydrogeological zone HZ19C, while OL-KR10, OL-KR15B, OL-KR16B, OL-KR17B, OL-KR18B are all directly connected by HZ19A. Therefore the analysis of possible connections via the sparsely fractured rock are limited to connections between the first group excluding OL-KR10 (i.e., OL-KR14, OL-KR15, OL-KR16, OL-KR17, OL-KR18) and the second group (OL-KR15B, OL-KR16B, OL-KR17B, OL-KR18B), rather than connections within either of these groups.

Results of automated curve-fitting

Automated curve-fitting according to the methods described above yields estimates of flow dimension and ancillary parameters as listed in Table 5.4. Fits of the GRF model to individual tests are plotted in Appendix 4.

The results are plotted in Figure 5.8 in terms of the cumulative distributions of flow dimensions for observation intervals with direct connections to the pumped well, vs. observation well without direct connections. As noted in section 2.2.2, the circumstances giving rise to sub-linear ($n < 1$) or hyperspherical ($n > 3$) flow cannot persist indefinitely, but can occur over the limited scale of a well test.

As for the previous case of a long-term pumping test in OL-KR24, the main difference that can be seen is that the flow dimensions for observation intervals with direct connections (mainly via HZ19A) tend to be close to cylindrical or 2-D flow, while observation intervals without such direct connections tend to exhibit higher flow dimensions.

For the observation intervals that yielded estimates of $n > 3.0$, the hydraulic conductivity estimate is generally low, with the exception of two intervals with very high assessed values of K, both of which are associated with a connection to OK-KR15 via HZ19C. These anomalous values likely represent local heterogeneity in HZ19C.

In both Table 5.2 (for the long-term pumping test in OL-KR24) and Table 5.4 (for the pumping tests

Table 5.3 Intersections of hydrogeological zones with drillholes used in pumping tests in OL-KR14 through OL-KR18.

Hydrogeological zone	Drillhole intersected	Top (m)	Bottom (m)
HZ19A	OL-KR10	39.8	41.8
	OL-KR15B	19.1	25.1
	OL-KR16B	17	19
	OL-KR17B	8	10
	OL-KR18B	31.3	33.3
HZ19C	OL-KR10	60.6	64.8
	OL-KR14	79	81
	OL-KR15	57.6	59.6
	OL-KR16	47.9	49.9
	OL-KR17	49.8	51.8
	OL-KR18	50.4	52.4
HZ20A	OL-KR10	260	262
	OL-KR16	151.6	153.6
HZ20B	OL-KR10	326.6	328.6

in OL-KR14 through OL-KR18) it appears that the hydraulic conductivity values estimated with the GRF method are inversely correlated to flow dimension. This can be seen directly in Figure 5.9. The estimates of specific storage show a weaker inverse correlation (Figure 5.10). The inverse correlation of hydraulic conductivity to flow dimension is also apparent for the subset of observation intervals that are not connected to the pumped interval directly via a hydrogeological zone (Figure 5.11), but less regular.

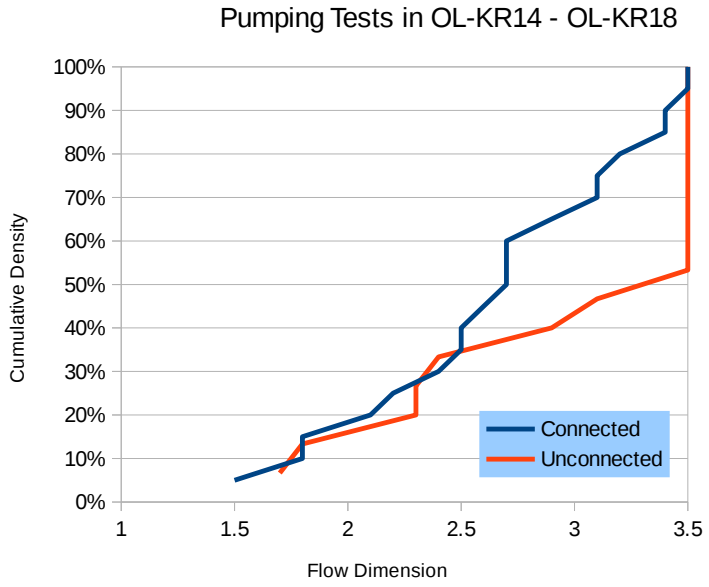

Figure 5.8. Cumulative distributions of flow dimensions estimated from responses to cross-hole pumping tests in OL-KR14 through OL-KR18.

Table 5.4. Results of automated curve-fitting of a generalized radial-flow model to responses to pumping tests in OL-KR14 through OL-KR18. Two connections that yielded anomalously high values of *K* are highlighted.

Pumping well	Monitoring section	Connection	Flow dimension *n*	Hydraulic conductivity *K* (m/s)	Specific storage S_s (1/m)
OL-KR18	OL-KR17	HZ19C	1.5	4.70E-005	2.34E-004
OL-KR17	OL-KR15	HZ19C	1.8	3.60E-006	2.34E-005
OL-KR18	OL-KR14	HZ19C	1.8	7.93E-006	1.76E-011
OL-KR17	OL-KR16	HZ19C	2.1	9.20E-007	5.35E-006
OL-KR14	OL-KR15	HZ19C	2.2	5.53E-007	4.49E-007
OL-KR14	OL-KR16	HZ19C	2.4	3.00E-007	5.62E-007
OL-KR14	OL-KR18	HZ19C	2.5	1.51E-007	1.04E-007
OL-KR16	OL-KR18	HZ19C	2.5	5.27E-007	2.46E-006
OL-KR18	OL-KR10	HZ19C	2.6	1.41E-007	2.26E-007
OL-KR16	OL-KR15	HZ19C	2.7	2.63E-007	9.91E-007
OL-KR17	OL-KR14	HZ19C	2.7	4.11E-008	3.58E-008
OL-KR18	OL-KR16	HZ19C	2.7	1.51E-007	1.85E-006
OL-KR16	OL-KR10	HZ19C	2.9	7.73E-008	1.23E-007
OL-KR15	OL-KR17	HZ19C	3.1	2.54E-002	1.59E-006
OL-KR16	OL-KR17	HZ19C	3.1	1.02E-006	1.22E-005
OL-KR17	OL-KR10	HZ19C	3.2	2.03E-008	2.53E-007
OL-KR16	OL-KR14	HZ19C	3.4	3.24E-009	1.37E-009
OL-KR18	OL-KR15	HZ19C	3.4	6.90E-002	3.07E-006
OL-KR14	OL-KR17	HZ19C	3.5	1.13E-007	6.32E-007
OL-KR15	OL-KR10	HZ19C	3.5	5.48E-008	1.11E-006
OL-KR15	OL-KR18	HZ19C	3.5	4.75E-009	3.38E-009
OL-KR18	OL-KR16B	none	1.7	2.88E-005	7.20E-012
OL-KR18	OL-KR15B	none	1.8	4.55E-006	1.63E-009
OL-KR14	OL-KR15B	none	2.3	5.20E-007	2.00E-006
OL-KR14	OL-KR16B	none	2.3	5.31E-007	2.11E-006
OL-KR14	OL-KR17B	none	2.4	3.76E-007	1.10E-006
OL-KR17	OL-KR15B	none	2.9	7.89E-008	1.46E-006
OL-KR17	OL-KR17B	none	3.1	6.79E-008	1.97E-006
OL-KR15	OL-KR15B	none	3.5	2.70E-009	1.68E-009
OL-KR15	OL-KR16	none	3.5	2.43E-009	1.23E-009
OL-KR15	OL-KR16B	none	3.5	2.68E-009	1.82E-009
OL-KR15	OL-KR17B	none	3.5	2.13E-009	8.62E-010
OL-KR16	OL-KR16B	none	3.5	2.23E-008	2.45E-007
OL-KR16	OL-KR17B	none	3.5	2.45E-008	2.86E-007

Results of prior interpretations of detailed cross-hole tests in ONK-PP262 and ONK-PP274

Detailed scale cross-hole tests carried out between intervals in ONK-PP262 and ONK-PP274 were entirely outside of the interpreted hydrogeological zones, and thus are likely to represent the properties of the sparsely-fractured rock. The interpretations of these data by Hansson et al. (2014) included generalized radial-flow models and thus are directly useful for the purposes of this evaluation, without re-analysis.

The results of these evaluation as plotted in Figure 5.12 show that more than 80% of the tests are in the range of cylindrical (2-D) to spherical (3-D) flow. Nearly 40% of the tests were evaluated as having flow dimensions of 3. Note that Hansson et al. (2014) capped the flow dimension at 3, unlike the analyses in the present study, which allowed higher flow dimensions.

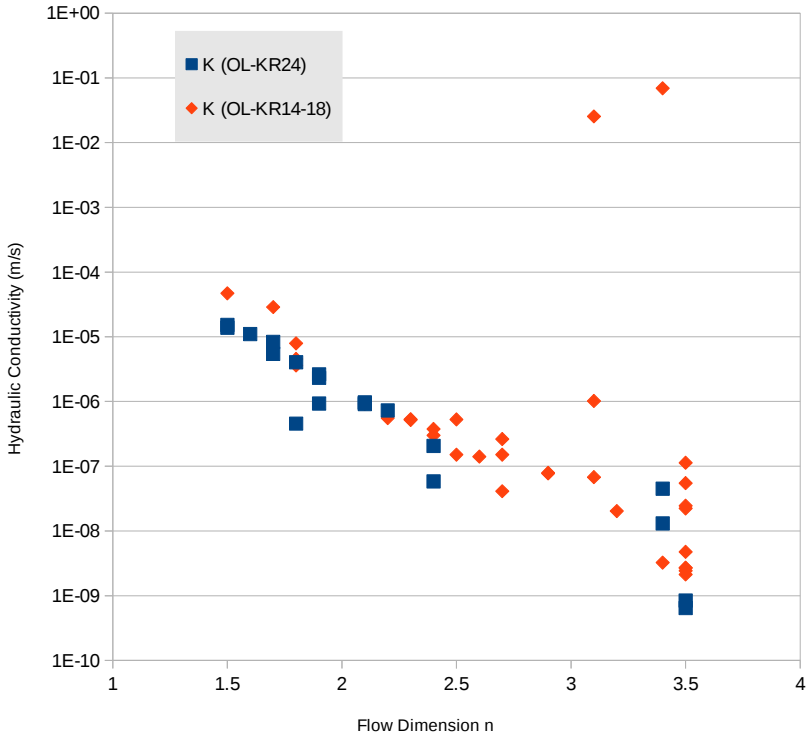

Figure 5.9. Correspondence of hydraulic conductivity *K* to flow dimension *n* based on generalized-radial flow evaluation of responses in pumping tests, according to the legend.

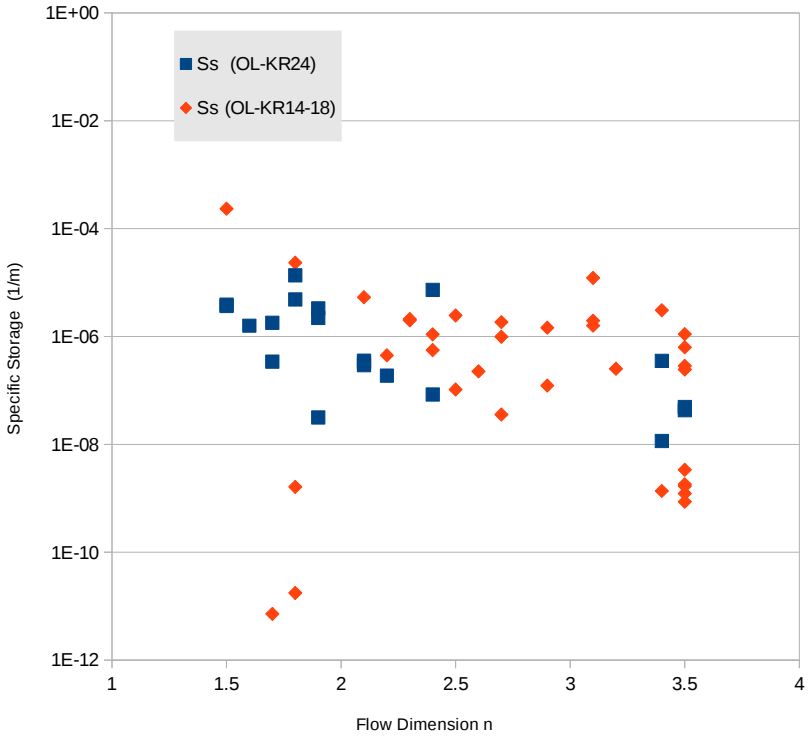

Figure 5.10. Correspondence of specific storage S_s to flow dimension *n* based on generalized-radial flow evaluation of responses in pumping tests, according to the legend.

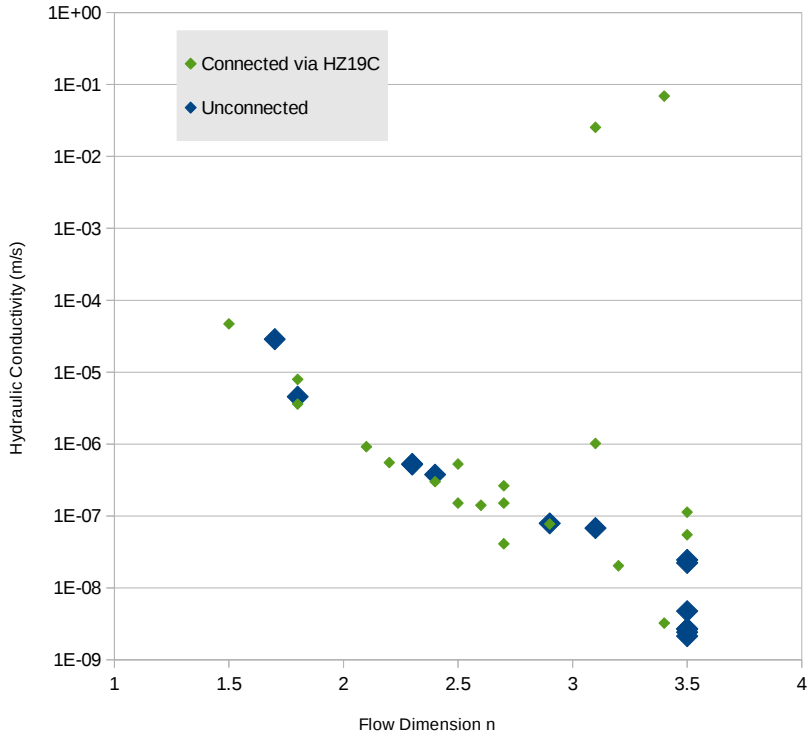

Figure 5.11. Correspondence of hydraulic conductivity *K* to flow dimension *n* based on generalized-radial flow evaluation of responses in pumping tests in OL-KR14 through OL-KR18, comparing cases of direct connections via hydrogeological zones vs. cases where there is no direct connection (so the observations are more likely to represent the sparsely fractured rock).

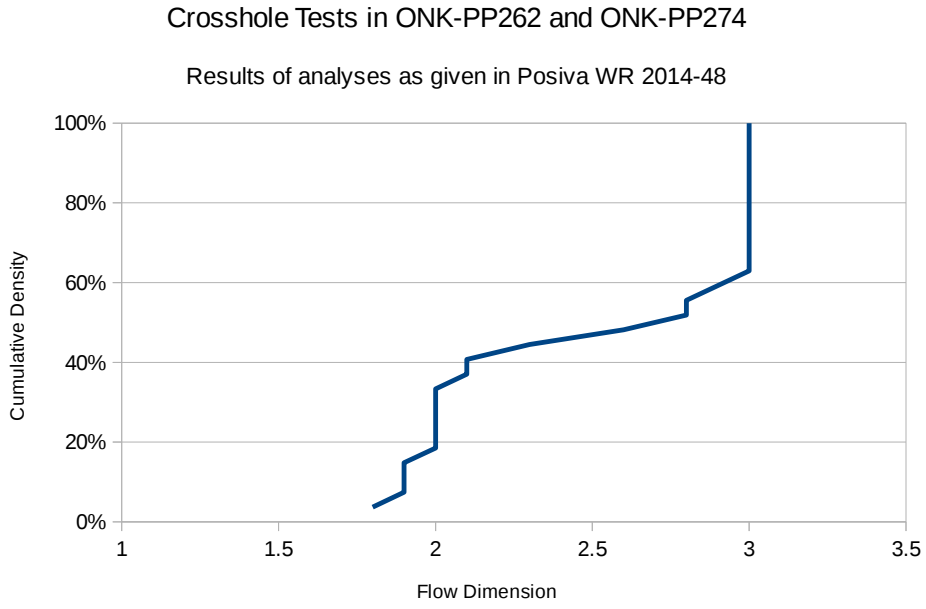

Figure 5.12. Cumulative distribution of flow dimensions estimated by Hansson et al. (2014) from responses to detailed-scale cross-hole pumping tests between packed-off sections of ONK-PP262 and ONK-PP274.

5.4 Sources of error

In the present analysis, the algorithm of Stehfest (1970) has been used for numerical inversion of the Laplace-transform solution. This algorithm is known to result in numerical instabilities depending on the choice of number of terms to evaluate, but it has the practical advantage in that the Laplace-transform solution $\bar{h}(r, s)$ only needs to be evaluated for real values of s.

More stable algorithms (e.g. the algorithms of Crump, 1976 and de Hoog et al., 1982) require evaluation of $\bar{h}(r, s)$ for complex values of s. The main challenge in applying these algorithms is in calculating the modified Bessel function $K_\nu(z)$. The results obtained here could be refined by using one of these algorithms in combination with the algorithms of Amos (1986) for calculating modified Bessel functions $K_\nu(z)$ for complex argument.

More important sources of error in estimating flow dimensions could be (1) the limited range of the data on the temporal scale, particularly the sparseness of data at early times, and (2) uncertainty in the effective starting time for some of the pumping tests (including uncertainty due to wellbore storage effects, which have not been taken into account).

6 Discussion

6.1 Indications of flow dimension based on responses in sparsely fractured rock

The results of GRF interpretation of the long-term pumping test in OL-KR24 indicate that the flow dimensions for observation intervals with direct connections via hydrogeological zones (mainly via HZ19A) exhibit flow that is close to cylindrical (2-D), while observation intervals without such direct connections tend to exhibit higher flow dimensions, indicative of more spherically divergent flow systems in the sparsely-fractured rock.

The results from intermediate-scale cross-hole tests in OL-KR14 through OL-KR18 are broadly similar. Again, flow dimensions for observation intervals with direct connections (mainly via HZ19A) tend to be close to cylindrical or 2-D flow, while observation intervals without such direct connections tend to exhibit higher flow dimensions, indicative of a more spherically divergent flow systems in the sparsely-fractured rock.

More detailed-scale cross-hole tests evaluated by Hansson et al. (2014) show that more than 80% of the tests are in the range of cylindrical (2-D) to spherical (3-D) flow. Thus on all three scales evaluated, the preponderance of results point toward a well-connected flow system that tends toward 2-D or 3-D behavior.

A strong inverse correlation between flow dimension and hydraulic conductivity, as seen in Tables 5.2 and 5.4 as well as in Figure 5.9. This inverse correlation is seen most strongly in the drillhole intervals that are connected via hydrogeological zones, but an inverse correlation is also seen in the intervals without such connections (Figure 5.11), which are more likely to represent the sparsely-fractured rock. The occurrence of sub-cylindrical flow in the highest-conductivity cases gives support to the idea that the strongest flow paths in the sparsely fractured rock are also sparsely connected.

6.2 Interpretation of flow system connectivity

As mentioned in the introductory section, the results of GRF interpretation of well-test data do not have an unambiguous interpretation in terms of flow system geometry. Provided that the time scale of the tests is sufficient to extend past the first few intersections, a well-connected system of pipe-like 1-D channels could yield the same quasi-spherical flow dimension as a well-connected system of plate-like fractures, or a locally homogeneous porous medium.

However, the preponderance of flow dimensions in the range of cylindrical to spherical flow, for intervals that are not connected directly by hydrogeological zones, is suggestive of a well-connected flow system that would not be expected if the flow system were best described by a sparse channel network. It should be cautioned that the behavior for solute transport could be different from the behavior for head or pressure propagation. However the results generally do not give strong positive support for the dominance of a sparsely connected flow system at the Olkiluoto site.

One seemingly contradictory line of evidence is the occurrence of a few pumping/observation-well connections, not explained by direct connections via a hydrogeological zone, which have high hydraulic conductivity but sub-cylindrical flow dimension. This suggests that the highest-conductivity flow paths through the sparsely-fractured rock could be more channel-like.

One model of the sparsely-fractured rock that could account for both these types of behavior is a well-connected network of mostly low-transmissivity fractures (accounting for the typical high flow dimensions but low K), within which there is a few persistent, higher-K channels.

6.3 Potential for further analyses of existing data

Data from routine monitoring of water levels and hydraulic heads in drillholes have not been used in the analysis, due to the long intervals (an hour or more) between data points for most drillholes.

For two of the surface-based drillholes with automatic monitoring of head (KR08 and KR27) and for the monitored drillholes in ONKALO, data are available for a slightly faster sampling rate (15 minutes), so the temporal resolution is improved by 0.6 order of magnitude. If localized perturbations (such as pumping in a particular drillhole e.g. to prepare for chemical sampling) with well-defined starting points and lasting for at least one day can be identified near these drillholes, additional interpretations could possibly be obtained.

In most such cases where the pumping rate is not strictly controlled, the responses would need to be evaluated by multi-rate superposition methods (Streltsova, 1988) as extended to the case of generalized-radial flow (Geier et al., 1996). Depending on the strength of the perturbation, filtering of time-varying effects of earth tides, atmospheric pressure variation, etc. might also be necessary. As the level of complexity of the analysis increases, uncertainty in the results would also tend to increase, so the marginal gain in information from such an evaluation might not motivate the required level of effort.

7 Conclusions

The results of generalized-radial flow interpretation of pumping tests generally indicate that flow between observation intervals with direct connections via hydrogeological zones (HZs) are close to cylindrical (2-D), although with variability that may reflect local heterogeneity in those zones.

Observation intervals without direct connections via HZs tend to exhibit higher flow dimensions, indicative of more spherically divergent flow systems in the sparsely-fractured rock. On the three different scales of cross-hole tests considered, the preponderance of results point toward a well-connected flow system that tends toward 2-D or 3-D behavior.

However a strong inverse correlation is seen between flow dimension and hydraulic conductivity, even in the intervals without direct connections via HZs that are thus more likely to represent the sparsely fractured rock. The occurrence of sub-cylindrical flow in the highest-conductivity cases gives support to the idea that the strongest flow paths in the sparsely fractured rock are also sparsely connected. This suggests that the highest-conductivity flow paths through the sparsely-fractured rock could be more channel-like.

One model of the sparsely-fractured rock that could account for both these types of behavior is a well-connected network of mostly low-transmissivity fractures, within which there is a few persistent, higher-conductivity channels.

8 References

Abramowitz, M. and Stegun, I.A., 1964. Handbook of Mathematical Functions with Formulas, Graphs, and Mathematical Tables, National Bureau of Standards.

Ahokas, H., Rouhiainen, P., Komulainen, J., and Pöllänen, J., 2014. Analysis of hydrogeological flow responses in Olkiluoto. Working Report 2014-14, Posiva Oy, Eurajoki, Finland.

Amos, D.E., 1986. A portable package for Bessel functions of complex argument and nonnegative order, ACM Transactions on Mathematical Software, Vol. 12, No. 3, p. 265–273.

Ball, J.K., Black, J.H., Brightman, M., and Doe, T., 1991. Large scale cross hole testing. Stripa Project Technical Report 91-17, Swedish Nuclear Fuel and Waste Management Co., Stockholm, Sweden.

Barker, J.A., 1988. A generalized radial-flow model for pumping tests in fractured rock, Water Resources Research, Vol. 24, pp. 1796–1804.

Black, J.H., Robinson, P.C., and Barker, J.A., 2006. A preliminary investigation of the concept of 'hyper-convergence' using 'sparse' channel networks. Report R-06-30, Swedish Nuclear Fuel and Waste Management Co., Stockholm, Sweden.

Chapman, N., Bath, A., Geier, J., and Stephansson, O., 2015. The disposal site and underground construction. STUK-TR 17. Radiation and Nuclear Safety Authority, Helsinki, Finland.

Crump, K.S., Numerical inversion of Laplace transforms using a Fourier series approximation, Journal of the Association of Computing Machinery, 23 (1976), p. 89–96.

de Hoog, F.R., Knight, J.H., Stokes, A.N., 1982. An improved method for numerical inversion of Laplace transforms. SIAM J. Sci. Stat. Comput., Vol. 3, No. 3, p. 357–366.

Doe, T.W. and Geier, J.E. 1990. Interpreting fracture system geometry using well test data, Stripa Project Technical Report 91-03, Swedish Nuclear Fuel and Waste Management Co., Stockholm, Sweden.

Geier, J.E., Doe, T.W., Benabderrahman, A., and Hässler, L., 1996. Generalized radial-flow interpretations of well tests for the SITE-94 Project. SKI Report 96:4, Swedish Nuclear Power Inspectorate, Stockholm, Sweden.

Hansson, K., Ludvigson, J-E., Nordqvist, R., Ragvald, J., and Andersson, P., 2014. Analysis of detailed hydraulic interference tests between Boreholes ONK-PP262 and ONK-PP274. Working Report 2014-48, Posiva Oy, Eurajoki, Finland.

Moreno, L., and Neretnieks, I., 1991. Fluid and solute transport in a network of channels. Technical Report 91-44, Swedish Nuclear Fuel and Waste Management Co, Stockholm.

Nelder, J.A. and Mead, R., 1965. A simplex method for function minimization. Computer Journal, Vol. 7, p. 308–313.

Press, W.H., Flannery, B.P., Teukolsky, S.A., and Vetterling, W.T., 1986. Numerical Recipes: The Art of Scientific Computing. Cambridge University Press, Cambridge, U.K.

Stehfest, H., 1970. Numerical inversion of Laplace transforms, Communications of the Association for Computing Machinery, Vol. 13, No. 1, p. 47–49.

Streltsova, T.D., 1988. Well Testing in Heterogeneous Formations, J. Wiley & Sons, New York, USA.

Theis, C.V., 1935. The relation between the lowering of the piezometric surface and the rate and duration of discharge of a well using ground-water storage. Transactions of the American Geophysical Union, Vol. 16, p. 519–524.

Vaittinen, T., Ahokas, H., Nummela, J., and Paulamäki, S. Hydrogeological structure model of the Olkiluoto site – Update in 2010. Working Report 2011-65, Posiva Oy, Eurajoki, Finland.

Vaittinen, T. and Pentti, E., 2013. Compilation and analysis of hydrogeological pressure responses to field activities in Olkiluoto during 2006–2009. Working Report 2013-34, Posiva Oy, Eurajoki, Finland.

Vaittinen, T., Ahokas, H., Komulainen, J., Nummela, J., Pentti, E., Tammisto, E., Turku, J., Karvonen, T., and Aro, S., 2013. Results of Monitoring at Olkiluoto in 2012 – Hydrology and Hydrogeology. Working Report 2013-43, Posiva Oy, Eurajoki, Finland.

Vaittinen, T., Ahokas, H., Komulainen, J., Nummela, J., Pentti, E., Tammisto, E., Turku, J., Karvonen, T., and Aro, S., 2014. Results of Monitoring at Olkiluoto in 2013 – Hydrology and Hydrogeology. Working Report 2014-43, Posiva Oy, Eurajoki, Finland.

Vaittinen, T., Ahokas, H., Komulainen, J., Nummela, J., Pentti, E., Tammisto, E., Turku, J., Karvonen, T., and Aro, S., 2015. Results of Monitoring at Olkiluoto in 2014 – Hydrology and Hydrogeology. Working Report 2015-43, Posiva Oy, Eurajoki, Finland.

Van Camp, M., and Vauterin, P., 2005. Tsoft: graphical and interactive software for the analysis of time series and earth tides. Computers & Geosciences, Vol. 31, No. 5, p. 631–640, doi:10.1016/j.cageo.2004.11.015.

APPENDIX 1 Mathematical derivation of well-test solutions for generalized radial flow

The generalized-radial flow equations of Barker (1988) are developed in terms of a system of *n*-dimensional, concentric spherical surfaces. The area of these surfaces varies with distance *r* from the center as:

$$A_c = \alpha_n r^{n-1}$$

and α_n is an n-dimensional angle defined by:

$$\alpha_n = \frac{2\pi^{n/2}}{\Gamma(n/2)}$$

and $\Gamma(z)$ is the gamma function of argument z. For the integral dimension cases, this *n*-dimensional angle takes values of $\alpha_1 = 2$, $\alpha_2 = 2\pi$, and $\alpha_3 = 4\pi$.

Using these relationships Barker (1988) developed a generalized radial flow equation:

$$\frac{K}{r^{n-1}}\frac{\partial}{\partial r}\left(r^{n-1}\frac{\partial h}{\partial r}\right) - S_s\frac{\partial h}{\partial t} = 0$$

where:

h	= hydraulic head	[L]
K_c	= hydraulic conductivity of the conduit	[LT^{-1}]
S_s	= specific storage of the conduit	[T^{-1}]

From this equation, solutions for specific types of situations arising in well test interpretation can be developed and used to compare with observed changes in heads and flowrates, as detailed in the next section.

The generalized radial-flow equation can be written in terms of hydraulic diffusivity $\eta = K/S_s$ as:

$$\frac{1}{r^{n-1}}\frac{\partial}{\partial r}\left(r^{n-1}\frac{\partial h}{\partial r}\right) - \frac{1}{\eta}\frac{\partial h}{\partial t} = 0$$

Application of the Laplace transformation to this equation gives:

$$\frac{d^2\bar{h}}{dr^2} + \frac{n-1}{r}\frac{d\bar{h}}{dr} - \frac{s}{\eta}\bar{h} = 0$$

where s is the Laplace transform variable. The general solution to this equation is a combination of modified Bessel functions of the first and second kinds, $I_v(z)$ and $K_v(z)$:

$$\bar{h}(r,s) = f_1(s)r^v K_v\left(r\sqrt{s/\eta}\right) + f_2(s)r^v I_v\left(r\sqrt{s/\eta}\right)$$

where $v = 1 - n/2$ and $f_1(s)$ and $f_2(s)$ are functions determined by a given set of boundary conditions.

In typical development of solutions for well test interpretation, the assumptions of uniform initial head:

$$h(r,t_0) = h_0$$

and that the perturbation becomes negligible at great distance from the pumping well:

$$\lim_{r\to\infty} h(r,t) = h_0$$

leads to a requirement that $f_2(s) = 0$, so the solution simplifies to:

$$\bar{h}(r,s) = f_1(s)r^v K_v\left(r\sqrt{s/\eta}\right)$$

and $f_1(s)$ is determined by the specified perturbation at the wellbore.

From this general solution, Laplace transform solutions for specific testing methods are readily derived as follows.

Constant-rate pumping test

When the perturbation takes the form of a pumping test in which a section of length b in a pumping well of radius rw is pumped at a constant rate:

$$Q(t) = Q_o, t > 0$$

The rate of change of water storage in the source is:

$$S_w\left(\frac{\partial h}{\partial t}\right)_{r=r_w} = Q(t) + Kb^{3-n}\alpha_n\pi r_w^{n-1}\left(\frac{\partial h}{\partial r}\right)_{r=r_w}$$

where S_w is the wellbore storage coefficient (volumetric storage per unit wellbore volume per unit increase in head).

The Laplace transform of the solution satisfying

this boundary condition is (Barker, 1988; Ball et al., 1991):

$$\bar{h}(r,s)=\frac{Q_o r^{\nu} r_w^{\ \nu} K_{\nu}\left(r\sqrt{s/\eta}\right)}{sKb^{3-n}\alpha_n \lambda K_{\nu-1}\left(r_w\sqrt{s/\eta}\right)}$$

Infinitesimal well

For the bounding case of an infinitesimal well (rw approaching 0), Barker (1988) obtained a closed-form solution:

$$h(r,t)=\frac{Q_o r^{2\nu}}{4\pi^{1-\nu}Kb^{3-n}}\Gamma(-\nu,u)$$

where:

$$u=\frac{r^2}{4\eta t}$$

and where $\Gamma(\nu,u)$ is the incomplete gamma function (Abramowitz and Stegun, 1964).

For the case ν = 1/2 (corresponding to flow dimension n = 1) this simplifies to:

$$h(r,t)=\frac{Q_o r}{4\sqrt{\pi}Kb^2}\Gamma\left(-\frac{1}{2},u\right)$$
$$=\frac{Q_o r}{2\sqrt{\pi}Kb^2}\left(\frac{e^{-u}}{\sqrt{u}}-\sqrt{\pi}\,\mathrm{erfc}\sqrt{u}\right)$$

where erfc(u) is the complementary error function:

$$\mathrm{erfc}(z)=\frac{2}{\sqrt{\pi}}\int_z^{\infty} e^{-t^2}dt$$

or the case ν = 0 (corresponding to flow dimension n = 2) this simplifies to:

$$h(r,t)=\frac{Q_o}{4\pi Kb}W(u)$$

where $W(u)$ is the well function of Theis (1935), also known in mathematical literature as the exponential integral function:

$$W(u)=\mathrm{Ei}(u)=-\int_{-u}^{\infty}\frac{e^x}{x}dx$$

For the case ν = –1/2 (corresponding to flow dimension n = 3) this simplifies to:

$$h(r,t)=\frac{Q_o r}{4\pi^{3/2}rK}\Gamma\left(-\frac{1}{2},u\right)=\frac{Q_o}{4\pi Kr}\mathrm{erfc}\sqrt{u}$$

where erfc(u) is complementary error function as arises in 1-D heat transport and other problems described by a 1-D diffusion equation.

Finite-diameter well

For the realistic case of a finite-diameter well, no closed-form solution is available. Therefore calculation of values of the function $h(r,t)$ corresponding to the Laplace-transform function of $\bar{h}(r, s)$ requires numerical inversion of the Laplace-transform solution:

$$\bar{h}(r,s)=\frac{Q_o r^{\nu} r_w^{\ \nu} K_{\nu}\left(r\sqrt{s/\eta}\right)}{sKb^{3-n}\alpha_n \lambda K_{\nu-1}\left(r_w\sqrt{s/\eta}\right)}.$$

In the present analysis, the algorithm of Stehfest (1970) has been used for numerical inversion of the Laplace-transform solution.

Constant-pressure injection test

Laplace-space solutions for the case of constant-pressure (or constant-head) injection tests were developed by Doe and Geier (1990) based on the general solution of Barker (1988). For the case of negligible skin effect and constant head hwo applied at the wellbore, the Laplace transform of flow rate into the rock is:

$$\bar{Q}(s)=h_{wo}Kb^{3-n}\alpha_n r_w^{n-2}\frac{\Phi\left(r_w\sqrt{s/\eta}\right)}{s}$$

where the function $\Phi_{\nu}(z)$ is defined as:

$$\Phi_{\nu}(z)=\frac{zK_{\nu-1}(z)}{K_{\nu}(z)}$$

and where $\eta = K/S_s$ is the hydraulic diffusivity.

APPENDIX 2 Intersections between drillholes and hydrogeological zones

Intersections of hydrogeological zones with drillholes were compiled from tables given by Vaittinen et al. (2011), as listed in the following table. The list includes hydrogeological zones that were included in the hydrogeological site model, as well as "possible" hydrogeological zones that were assessed as being either "high confidence" or "medium confidence."

Table A2. Intersections of hydrogeological zones with drillholes according to Vaittinen et al. (2011).

Drillhole	Zone	Top (m)	Bottom (m)	Source in Vaittinen et al. (2011)	Confidence level
OL-KR01	HZ20B	99	169.5	Table 5-6	Included in model
OL-KR01	HZ20A	105.9	114.3	Table 5-5	Included in model
OL-KR01	HZ099	525.9	527.9	Table 5-9	Included in model
OL-KR01	HZ21	610.3	619.2	Table 5-7	Included in model
OL-KR01	HZ21B	610.3	619.2	Table 5-8	Included in model
OL-KR02	HZ099	504	508	Table 5-9	Included in model
OL-KR02	HZ21	595.8	613	Table 5-7	Included in model
OL-KR02	HZ21B	595.8	613	Table 5-8	Included in model
OL-KR04	HZ19A	80.5	84.1	Table 5-2	Included in model
OL-KR04	HZ19C	115	117.8	Table 5-3	Included in model
OL-KR04	HZ19B	140.6	142.6	Table 5-4	Included in model
OL-KR04	HZ20A	306.2	314.9	Table 5-5	Included in model
OL-KR04	HZ20B	365.3	367.3	Table 5-6	Included in model
OL-KR04	HZ21	756.8	764.2	Table 5-7	Included in model
OL-KR04	BFZ161	808.3	809.95	Table 5-17	Medium Confidence
OL-KR04	HZ21B	862.9	864.9	Table 5-8	Included in model
OL-KR05	HZ20A	42	44	Table 5-5	Included in model
OL-KR05	HZ001	202.6	206.6	Table 5-10	Included in model
OL-KR05	HZ099	278	284	Table 5-9	Included in model
OL-KR05	HZ21B	404.3	410.3	Table 5-8	Included in model
OL-KR05	HZ21	465.5	485.5	Table 5-7	Included in model
OL-KR06	HZ099	126	132.2	Table 5-9	Included in model
OL-KR06	HZ001	134.7	136.7	Table 5-10	Included in model
OL-KR06	HZ21B	393.3	400.3	Table 5-8	Included in model
OL-KR06	HZ21	473.6	477.9	Table 5-7	Included in model
OL-KR07	HZ19B	46.9	48.8	Table 5-4	Included in model
OL-KR07	HZ20A	224.2	249.9	Table 5-5	Included in model
OL-KR07	HZ20B	279.6	287.1	Table 5-6	Included in model
OL-KR07	HZ21	689.5	711.6	Table 5-7	Included in model
OL-KR08	HZ19A	80.6	83.3	Table 5-2	Included in model
OL-KR08	HZ19C	106	114.8	Table 5-3	Included in model
OL-KR08	HZ19B	249.1	255.9	Table 5-4	Included in model
OL-KR08	HZ20A	451.7	454.5	Table 5-5	Included in model
OL-KR08	HZ20B	547.6	561	Table 5-6	Included in model
OL-KR09	HZ19C	146.3	151.1	Table 5-3	Included in model
OL-KR09	HZ20A	443.2	446	Table 5-5	Included in model
OL-KR09	HZ20B	468.6	480	Table 5-6	Included in model

Drillhole	Zone	Top (m)	Bottom (m)	Source in Vaittinen et al. (2011)	Confidence level
OL-KR09	BFZ175	547.74	549.23	Table 5-17	High Confidence
OL-KR10	HZ19A	39.8	41.8	Table 5-2	Included in model
OL-KR10	HZ19C	60.6	64.8	Table 5-3	Included in model
OL-KR10	HZ20A	260	262	Table 5-5	Included in model
OL-KR10	HZ20B	326.6	328.6	Table 5-6	Included in model
OL-KR11	HZ19C	121.8	123.8	Table 5-3	Included in model
OL-KR11	BFZ175	413.08	413.27	Table 5-17	High Confidence
OL-KR11	HZ21	623.6	627.1	Table 5-7	Included in model
OL-KR12	HZ19C	42	46.5	Table 5-3	Included in model
OL-KR12	HZ099	579.7	585.6	Table 5-9	Included in model
OL-KR12	HZ21	651.3	672.4	Table 5-7	Included in model
OL-KR12	HZ21B	737.3	751.4	Table 5-8	Included in model
OL-KR13	HZ001	362.4	364.4	Table 5-10	Included in model
OL-KR13	HZ099	450.3	459.9	Table 5-9	Included in model
OL-KR14	HZ19A	50	52	Table 5-2	Included in model
OL-KR14	HZ19C	79	81	Table 5-3	Included in model
OL-KR15	HZ19C	57.6	59.6	Table 5-3	Included in model
OL-KR15B	HZ19A	19.1	25.1	Table 5-2	Included in model
OL-KR16	HZ19C	47.9	49.9	Table 5-3	Included in model
OL-KR16	HZ20A	151.6	153.6	Table 5-5	Included in model
OL-KR16B	HZ19A	17	19	Table 5-2	Included in model
OL-KR17	HZ19C	49.8	51.8	Table 5-3	Included in model
OL-KR17B	HZ19A	8	10	Table 5-2	Included in model
OL-KR18	HZ19C	50.4	52.4	Table 5-3	Included in model
OL-KR18B	HZ19A	31.3	33.3	Table 5-2	Included in model
OL-KR19	HZ001	202	214	Table 5-10	Included in model
OL-KR19	HZ099	253	261	Table 5-9	Included in model
OL-KR19	HZ21	456.7	466	Table 5-7	Included in model
OL-KR19	HZ21B	456.7	466	Table 5-8	Included in model
OL-KR20	HZ20A	109.4	111.4	Table 5-5	Included in model
OL-KR20	HZ20B	138	142	Table 5-6	Included in model
OL-KR20	HZ099	416	429	Table 5-9	Included in model
OL-KR20	HZ099	468	470	Table 5-9	Included in model
OL-KR22	HZ19A	96.1	102.7	Table 5-2	Included in model
OL-KR22	HZ19C	108.3	113.2	Table 5-3	Included in model
OL-KR22	HZ19B	146.9	152.7	Table 5-4	Included in model
OL-KR22	BFZ100	337.7	340.5	Table 5-14	Included in model
OL-KR22	HZ20A	390.4	392.4	Table 5-5	Included in model
OL-KR22	HZ20B	423	426.4	Table 5-6	Included in model
OL-KR23	HZ19A	88.7	94.7	Table 5-2	Included in model
OL-KR23	HZ19C	135.2	137.2	Table 5-3	Included in model
OL-KR23	HZ19B	192.8	197	Table 5-4	Included in model
OL-KR23	BFZ100	372.5	373	Table 5-14	Included in model
OL-KR23	HZ20A	425.9	430	Table 5-5	Included in model
OL-KR24	HZ19A	93	95.3	Table 5-2	Included in model
OL-KR24	HZ19C	114.5	116.8	Table 5-3	Included in model
OL-KR24	HZ19B	114.5	116.8	Table 5-4	Included in model

Drillhole	Zone	Top (m)	Bottom (m)	Source in Vaittinen et al. (2011)	Confidence level
OL-KR24	HZ20A	303.6	306	Table 5-5	Included in model
OL-KR24	HZ20B	396	398.3	Table 5-6	Included in model
OL-KR25	HZ19A	58.6	64.6	Table 5-2	Included in model
OL-KR25	HZ19C	94.6	97.5	Table 5-3	Included in model
OL-KR25	HZ19B	123.3	125.3	Table 5-4	Included in model
OL-KR25	BFZ100	216.5	222.1	Table 5-14	Included in model
OL-KR25	HZ20A	342.6	352.5	Table 5-5	Included in model
OL-KR25	HZ20B	405.5	408.8	Table 5-6	Included in model
OL-KR26	BFZ100	95.8	98.3	Table 5-14	Included in model
OL-KR27	HZ19A	129	133	Table 5-2	Included in model
OL-KR27	HZ19C	207	211	Table 5-3	Included in model
OL-KR27	HZ19B	256.8	262.7	Table 5-4	Included in model
OL-KR27	HZ20A	503.8	505.8	Table 5-5	Included in model
OL-KR27B	HZ146	9.3	11.3	Table 5-11	Included in model
OL-KR28	HZ19A	134	140	Table 5-2	Included in model
OL-KR28	HZ19C	155.4	159.4	Table 5-3	Included in model
OL-KR28	HZ19B	170	180.2	Table 5-4	Included in model
OL-KR28	BFZ100	177.02	178.02	Table 5-14	Included in model
OL-KR28	HZ20A	388.3	390.8	Table 5-5	Included in model
OL-KR28	HZ20B	442.9	447.2	Table 5-6	Included in model
OL-KR29	HZ19A	62	64	Table 5-2	Included in model
OL-KR29	HZ19C	96	98	Table 5-3	Included in model
OL-KR29	HZ20A	167	175.2	Table 5-5	Included in model
OL-KR29	HZ20B	320.6	340.9	Table 5-6	Included in model
OL-KR29	HZ039	565.5	570	Table 5-13	Included in model
OL-KR29	HZ21	776.9	781.7	Table 5-7	Included in model
OL-KR30	HZ19A	50.7	54.7	Table 5-2	Included in model
OL-KR30	HZ19C	81.6	83.6	Table 5-3	Included in model
OL-KR31	HZ19A	101.4	109.4	Table 5-2	Included in model
OL-KR31	HZ19C	143.4	145.4	Table 5-3	Included in model
OL-KR31	HZ19B	174	176	Table 5-4	Included in model
OL-KR33	HZ001	150.2	152.2	Table 5-10	Included in model
OL-KR34	BFZ100	48.4	53.8	Table 5-14	Included in model
OL-KR34	HZ19A	60.7	79.3	Table 5-2	Included in model
OL-KR35	HZ19A	69.1	78.8	Table 5-2	Included in model
OL-KR36	HZ19A	84.5	95.4	Table 5-2	Included in model
OL-KR36	HZ19C	153.9	156.9	Table 5-3	Included in model
OL-KR37	BFZ100	56.2	57.5	Table 5-14	Included in model
OL-KR37	HZ19A	122.8	125.8	Table 5-2	Included in model
OL-KR37	HZ19C	171	175.1	Table 5-3	Included in model
OL-KR37	HZ19B	195.2	197.2	Table 5-4	Included in model
OL-KR38	HZ19A	87.2	89.6	Table 5-2	Included in model
OL-KR38	HZ19C	119.6	122.5	Table 5-3	Included in model
OL-KR38	HZ19B	119.6	122.5	Table 5-4	Included in model
OL-KR38	HZ20A	306.6	309.2	Table 5-5	Included in model
OL-KR38	HZ20B	378.7	391.6	Table 5-6	Included in model
OL-KR39	HZ20A	108	111.2	Table 5-5	Included in model

Drillhole	Zone	Top (m)	Bottom (m)	Source in Vaittinen et al. (2011)	Confidence level
OL-KR39	HZ20B	147.2	151.7	Table 5-6	Included in model
OL-KR40	HZ19C	284	284.5	Table 5-3	Included in model
OL-KR40	BFZ159	385.4	386.4	Table 5-17	Medium Confidence
OL-KR40	HZ20B	605.2	612.9	Table 5-6	Included in model
OL-KR40	HZ21	966.8	968.8	Table 5-7	Included in model
OL-KR40B	HZ146	4.9	6.9	Table 5-11	Included in model
OL-KR42	HZ19C	83.6	89.6	Table 5-3	Included in model
OL-KR42	BFZ100	183	198.8	Table 5-14	Included in model
OL-KR42	BFZ175	297.99	298.36	Table 5-17	High Confidence
OL-KR43	HZ001	58	60	Table 5-10	Included in model
OL-KR43	HZ21	339.6	343.3	Table 5-7	Included in model
OL-KR43	HZ008	571.6	592.9	Table 5-12	Included in model
OL-KR44	HZ19A	99.2	107.1	Table 5-2	Included in model
OL-KR44	HZ19C	117.1	125.2	Table 5-3	Included in model
OL-KR44	HZ20B	652.1	654.1	Table 5-6	Included in model
OL-KR44	BFZ152	793.3	793.68	Table 5-17	Medium Confidence
OL-KR45	BFZ152	68.89	69.16	Table 5-17	Medium Confidence
OL-KR45	HZ146	119.6	121.6	Table 5-11	Included in model
OL-KR45	BFZ160	176.02	180.51	Table 5-17	Medium Confidence
OL-KR46	HZ19C	84.3	86.3	Table 5-3	Included in model
OL-KR46	BFZ175	411.7	412.17	Table 5-17	High Confidence
OL-KR47	BFZ175	220.87	221.5	Table 5-17	High Confidence
OL-KR47	HZ21	524.6	555.4	Table 5-7	Included in model
OL-KR48	HZ19A	95.1	97.1	Table 5-2	Included in model
OL-KR48	HZ19C	106.2	108.2	Table 5-3	Included in model
OL-KR48	HZ19B	106.2	108.2	Table 5-4	Included in model
OL-KR48	HZ20A	297.4	299.4	Table 5-5	Included in model
OL-KR48	HZ20B	377.7	383.9	Table 5-6	Included in model
OL-KR49	HZ146	349.1	376.6	Table 5-11	Included in model
OL-KR50	HZ146	438.8	448	Table 5-11	Included in model
OL-KR51	HZ146	434.4	450.7	Table 5-11	Included in model
OL-KR52	HZ146	405.2	427.4	Table 5-11	Included in model
OL-PH01	BFZ100	151.6	154.3	Table 5-14	Included in model
ONK-PH04	BFZ100	27.1	29.6	Table 5-14	Included in model
ONK-PH04	HZ19A	84	86	Table 5-2	Included in model
ONK-PH05	HZ19C	56	58	Table 5-3	Included in model
ONK-PH05	HZ19B	172	176	Table 5-4	Included in model
ONK-PH08	HZ20A	50.9	52.9	Table 5-5	Included in model
ONK-PH09	HZ20B	38.4	40.4	Table 5-6	Included in model

APPENDIX 3 Detailed results of automatic curve-fitting to long-term pumping test in OL-KR24

A3.1 Results for Cluster 1

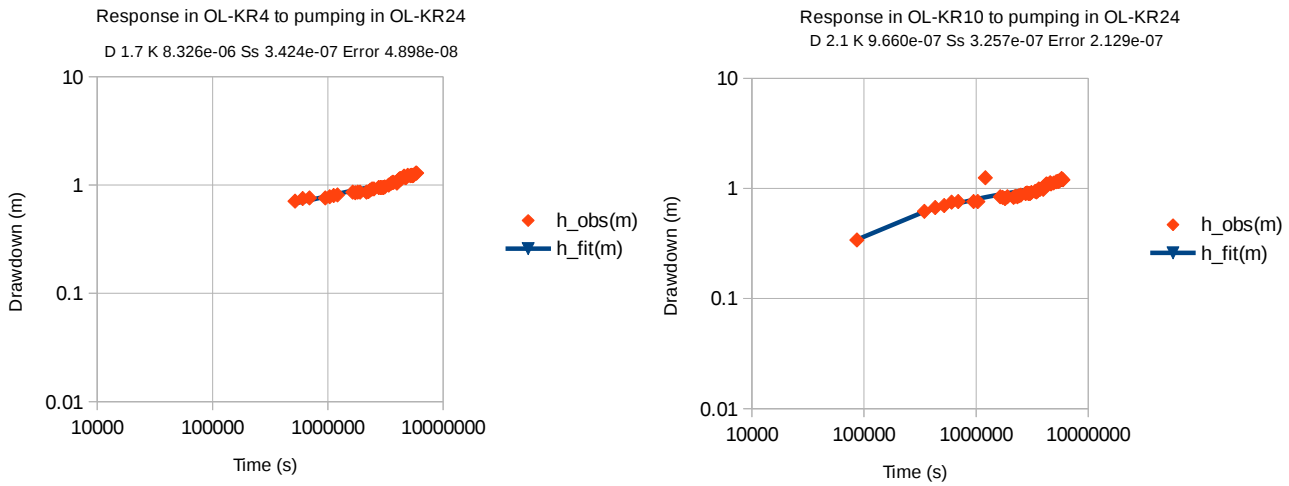

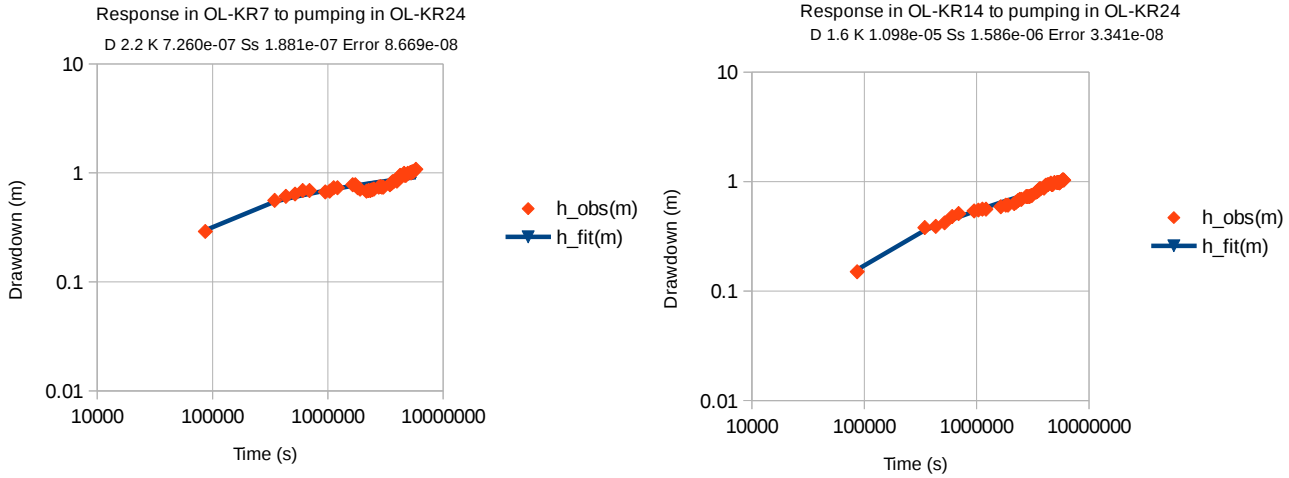

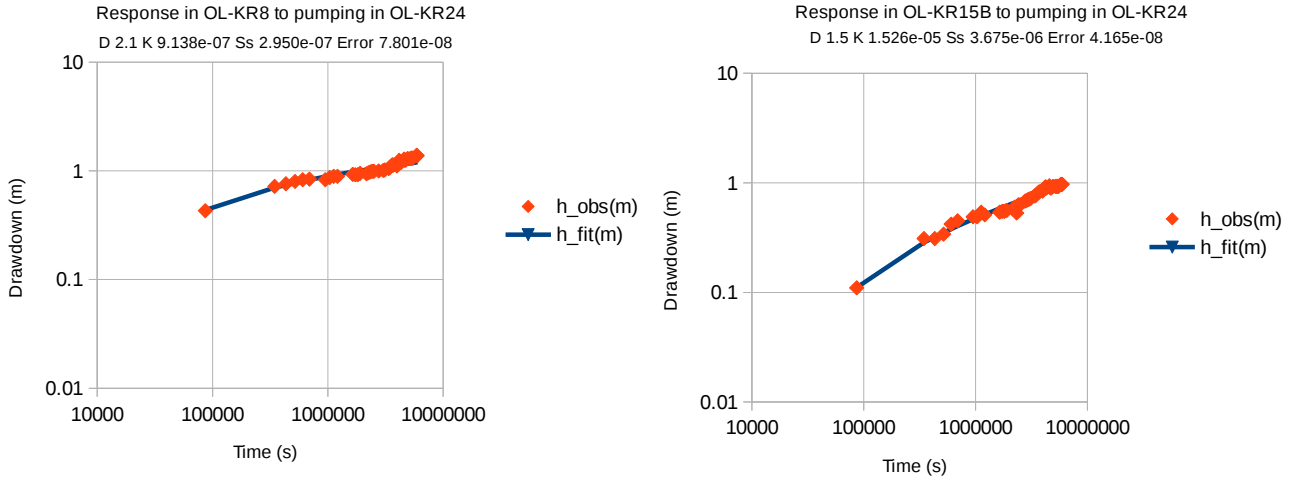

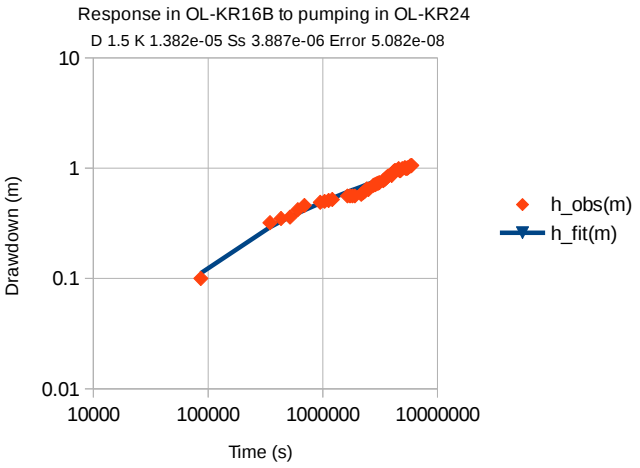
Response in OL-KR16B to pumping in OL-KR24
D 1.5 K 1.382e-05 Ss 3.887e-06 Error 5.082e-08
Drawdown (m)
10
1
0.1
0.01
10000
100000
1000000
10000000
Time (s)
h_obs(m)
h_fit(m)

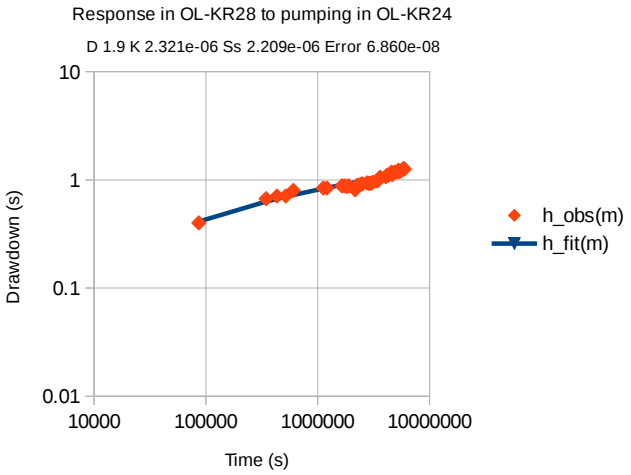
Response in OL-KR28 to pumping in OL-KR24
D 1.9 K 2.321e-06 Ss 2.209e-06 Error 6.860e-08
Drawdown (s)
10
1
0.1
0.01
10000
100000
1000000
10000000
Time (s)
h_obs(m)
h_fit(m)

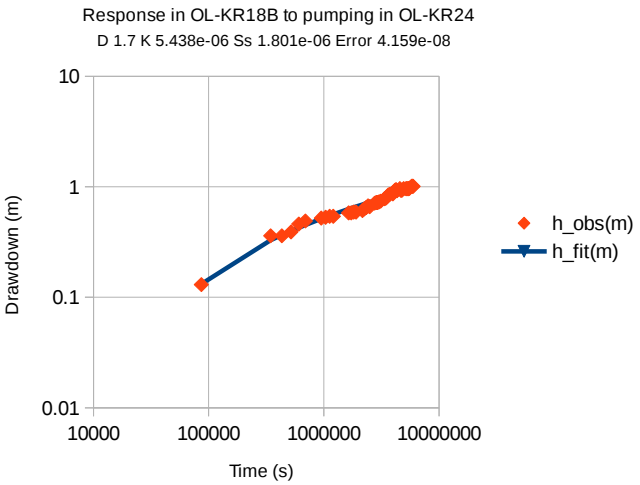
Response in OL-KR18B to pumping in OL-KR24
D 1.7 K 5.438e-06 Ss 1.801e-06 Error 4.159e-08
Drawdown (m)
10
1
0.1
0.01
10000
100000
1000000
10000000
Time (s)
h_obs(m)
h_fit(m)

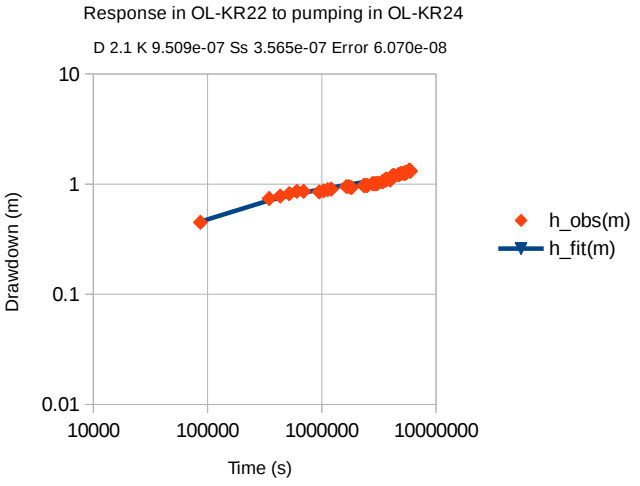
Response in OL-KR22 to pumping in OL-KR24
D 2.1 K 9.509e-07 Ss 3.565e-07 Error 6.070e-08
Drawdown (m)
10
1
0.1
0.01
10000
100000
1000000
10000000
Time (s)
h_obs(m)
h_fit(m)

A3.2 Results for Group 2

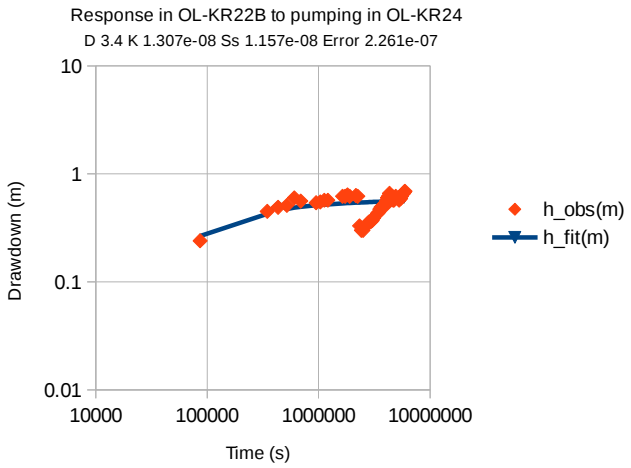

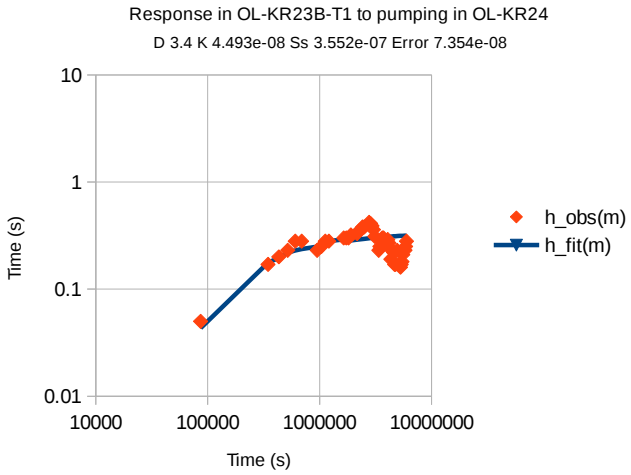

A3.3 Results for Cluster 3

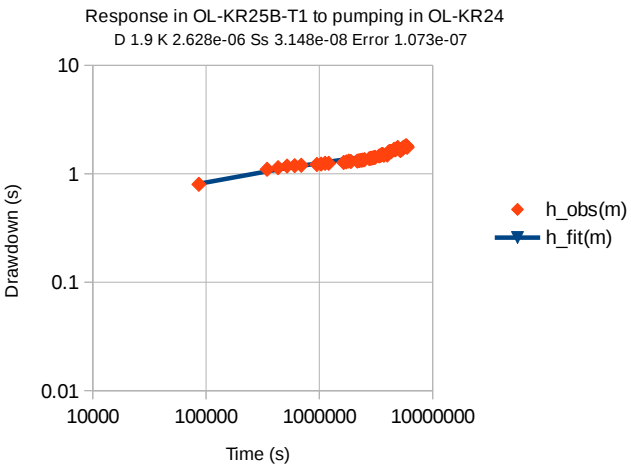

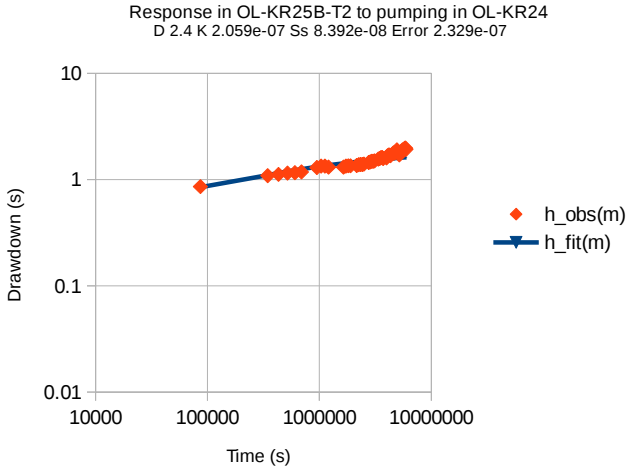

A3.4 Results for Cluster 4

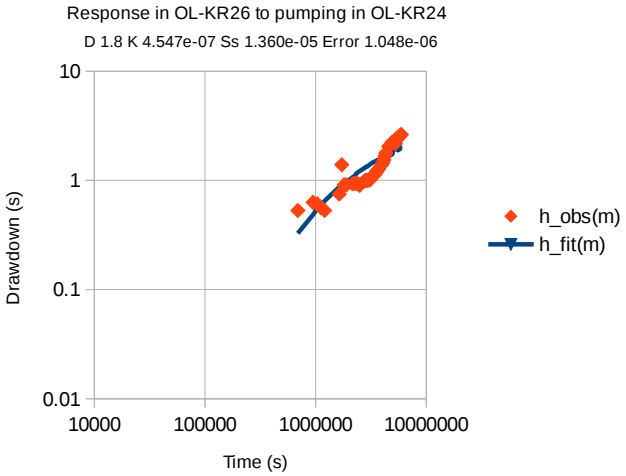

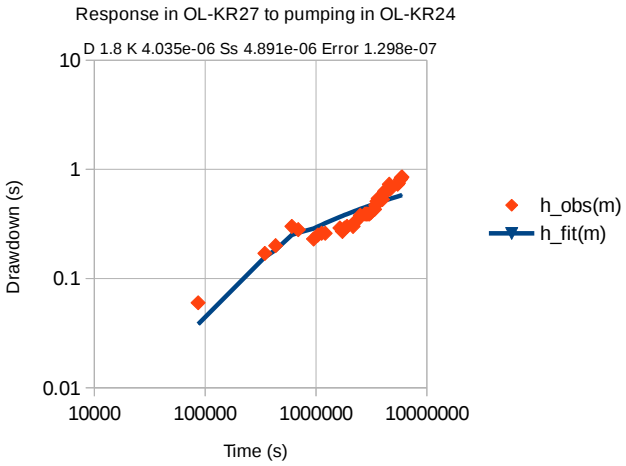

A3.5 Results for Group 5

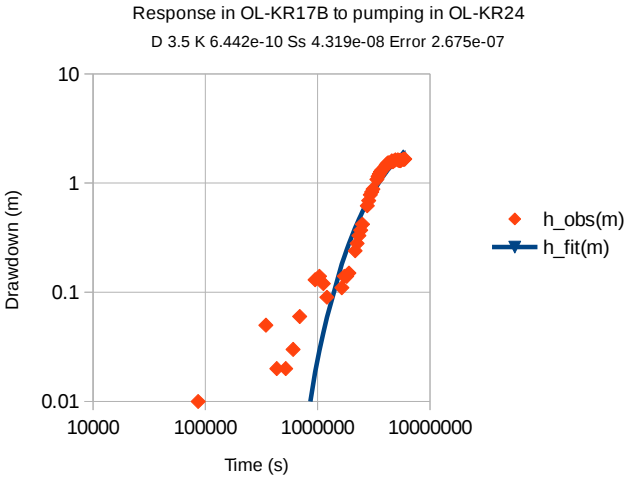

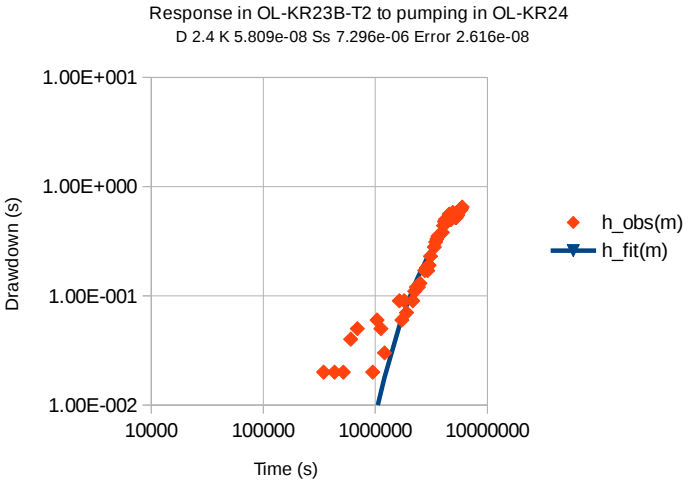

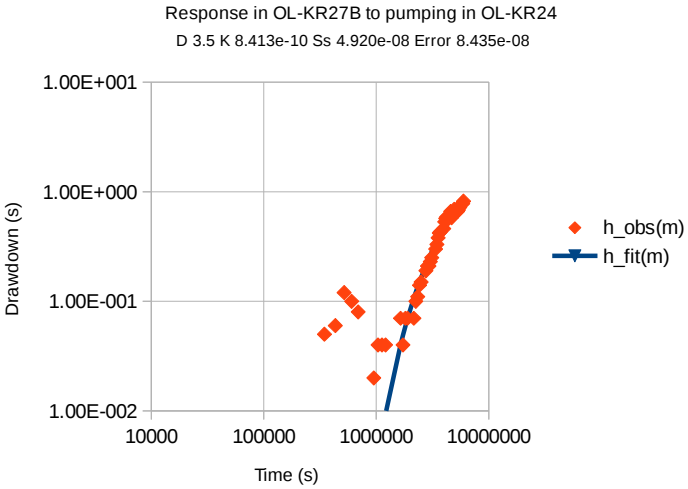

APPENDIX 4 Detailed results of automatic curve-fitting to cross-hole tests in OL-KR14–KR18

The following plots give the results of automated fitting of the generalized radial-flow model for the cross-hole tests in OL-KR14 through OL-KR18. Note that one plot is included for which the automated fitting failed; this was not used for the further analysis.

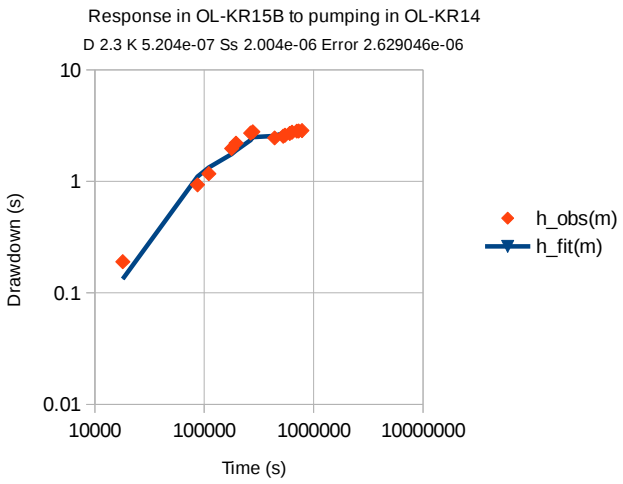

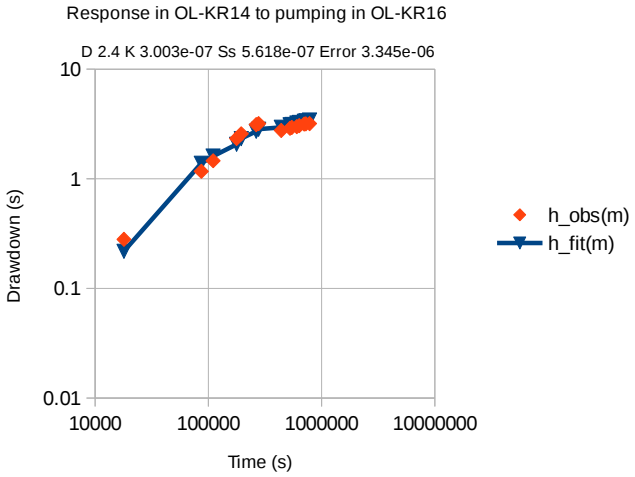

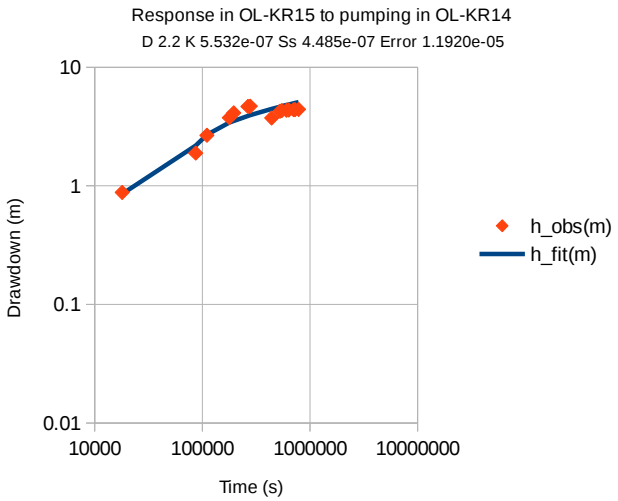

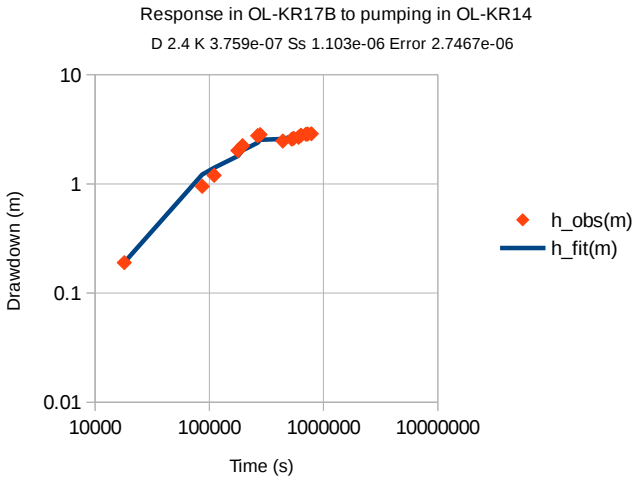

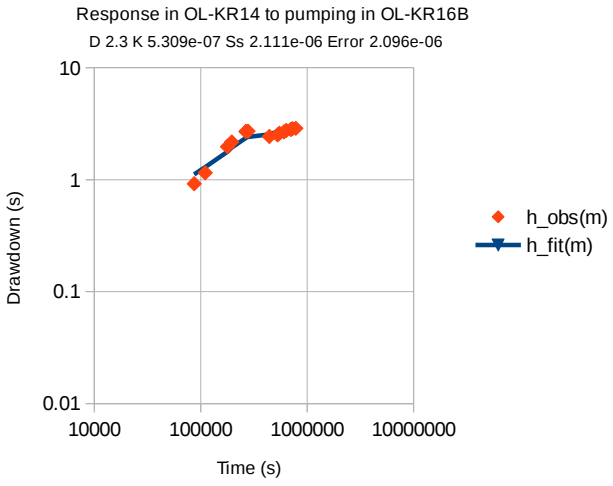

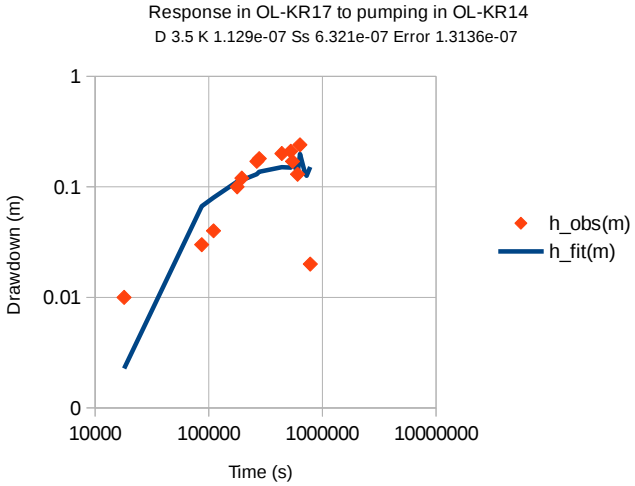

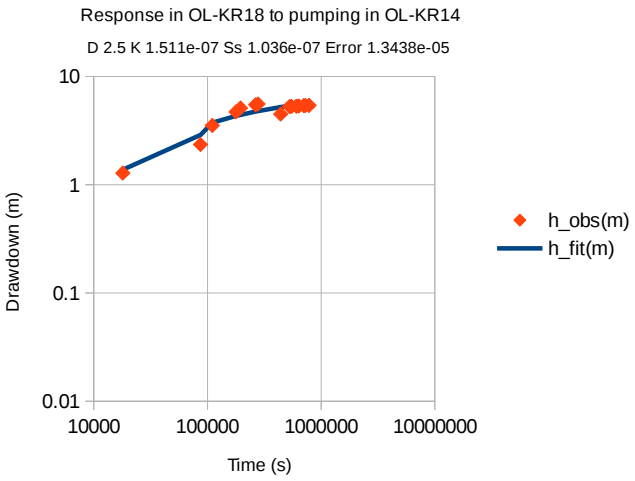
Response in OL-KR18 to pumping in OL-KR14
D 2.5 K 1.511e-07 Ss 1.036e-07 Error 1.3438e-05
Drawdown (m)
Time (s)
h_obs(m)
h_fit(m)

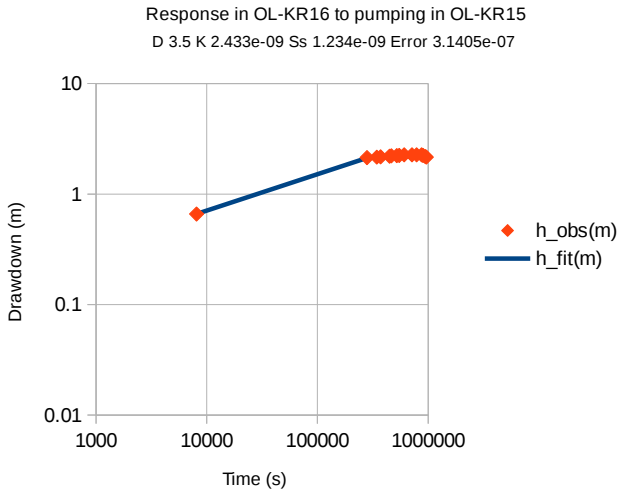
Response in OL-KR16 to pumping in OL-KR15
D 3.5 K 2.433e-09 Ss 1.234e-09 Error 3.1405e-07
Drawdown (m)
Time (s)
h_obs(m)
h_fit(m)

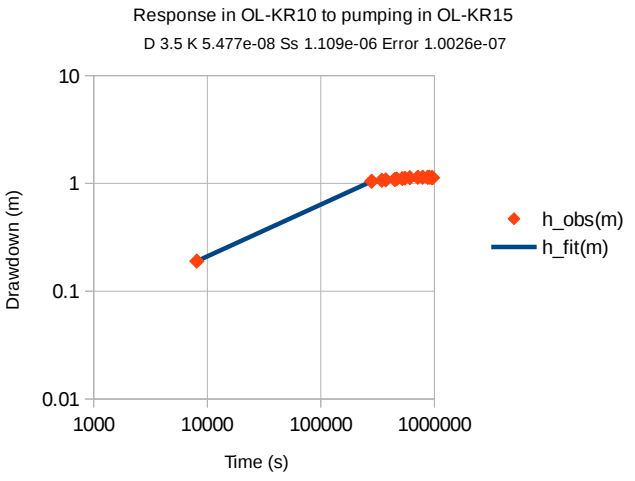
Response in OL-KR10 to pumping in OL-KR15
D 3.5 K 5.477e-08 Ss 1.109e-06 Error 1.0026e-07
Drawdown (m)
Time (s)
h_obs(m)
h_fit(m)

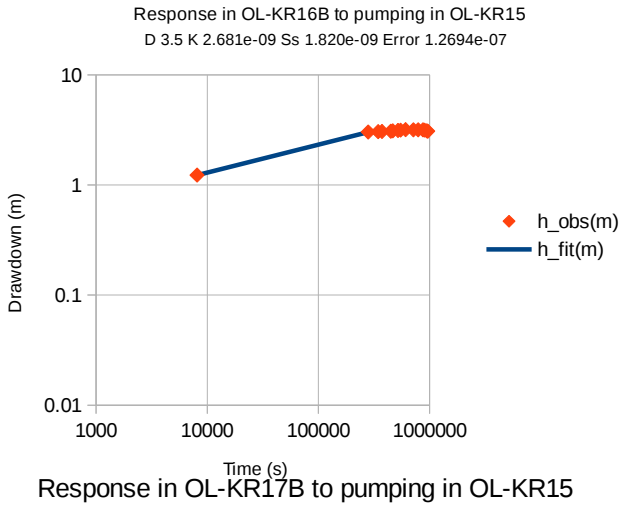
Response in OL-KR16B to pumping in OL-KR15
D 3.5 K 2.681e-09 Ss 1.820e-09 Error 1.2694e-07
Drawdown (m)
Time (s)
h_obs(m)
h_fit(m)

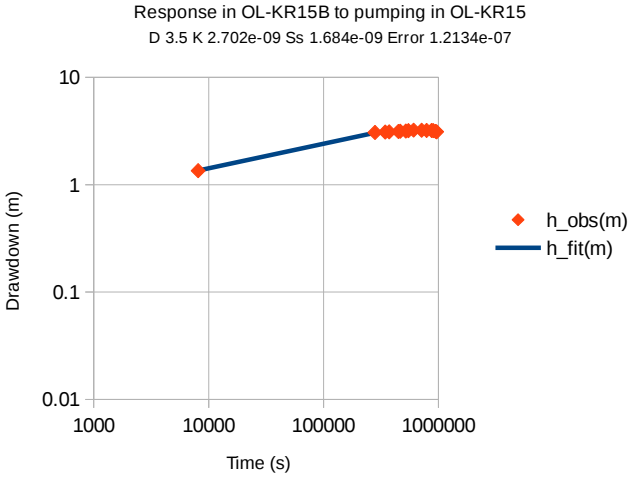
Response in OL-KR15B to pumping in OL-KR15
D 3.5 K 2.702e-09 Ss 1.684e-09 Error 1.2134e-07
Drawdown (m)
Time (s)
h_obs(m)
h_fit(m)

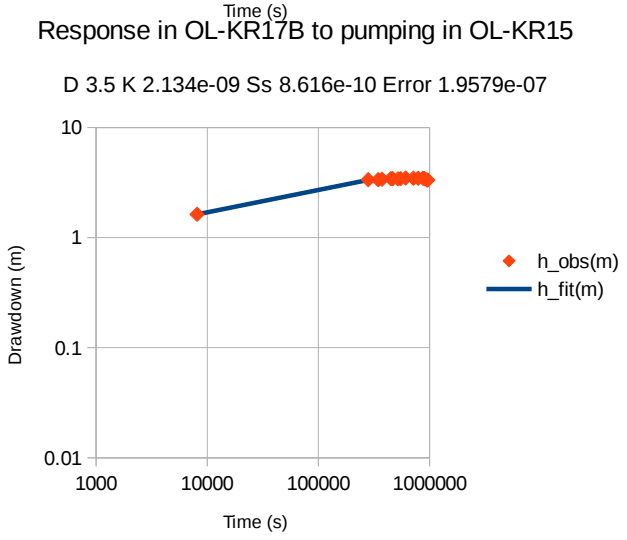
Response in OL-KR17B to pumping in OL-KR15
D 3.5 K 2.134e-09 Ss 8.616e-10 Error 1.9579e-07
Drawdown (m)
Time (s)
h_obs(m)
h_fit(m)

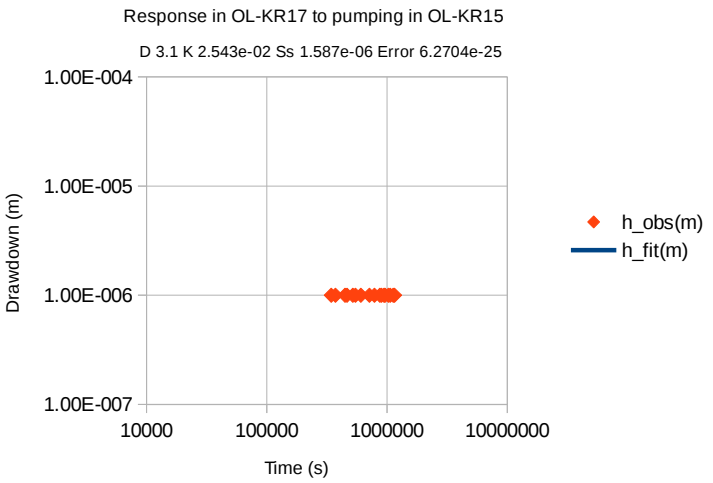
Response in OL-KR17 to pumping in OL-KR15
D 3.1 K 2.543e-02 Ss 1.587e-06 Error 6.2704e-25
1.00E-004
1.00E-005
1.00E-006
1.00E-007
Drawdown (m)
10000
100000
1000000
10000000
Time (s)
h_obs(m)
h_fit(m)

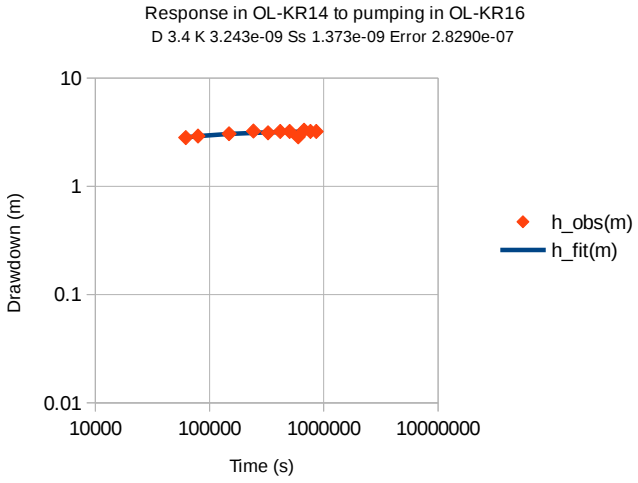
Response in OL-KR14 to pumping in OL-KR16
D 3.4 K 3.243e-09 Ss 1.373e-09 Error 2.8290e-07
10
1
0.1
0.01
Drawdown (m)
10000
100000
1000000
10000000
Time (s)
h_obs(m)
h_fit(m)

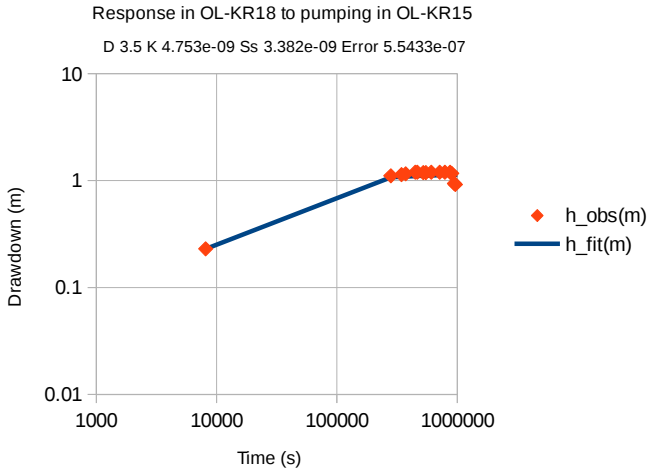
Response in OL-KR18 to pumping in OL-KR15
D 3.5 K 4.753e-09 Ss 3.382e-09 Error 5.5433e-07
10
1
0.1
0.01
Drawdown (m)
1000
10000
100000
1000000
Time (s)
h_obs(m)
h_fit(m)

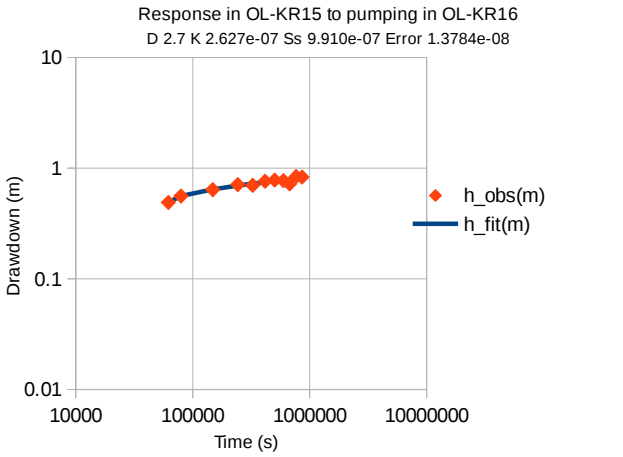
Response in OL-KR15 to pumping in OL-KR16
D 2.7 K 2.627e-07 Ss 9.910e-07 Error 1.3784e-08
10
1
0.1
0.01
Drawdown (m)
10000
100000
1000000
10000000
Time (s)
h_obs(m)
h_fit(m)

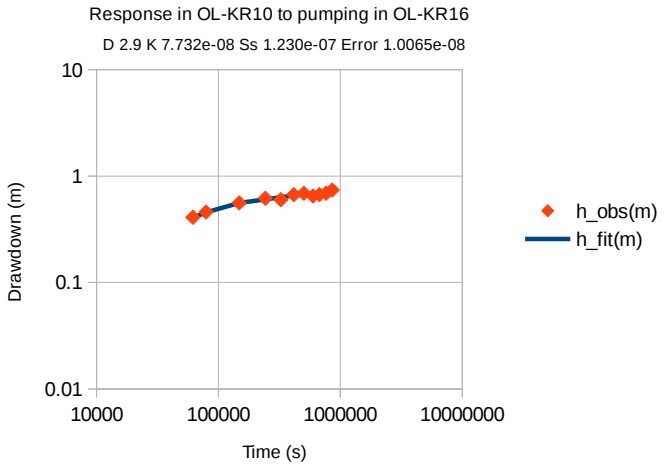
Response in OL-KR10 to pumping in OL-KR16
D 2.9 K 7.732e-08 Ss 1.230e-07 Error 1.0065e-08
10
1
0.1
0.01
Drawdown (m)
10000
100000
1000000
10000000
Time (s)
h_obs(m)
h_fit(m)

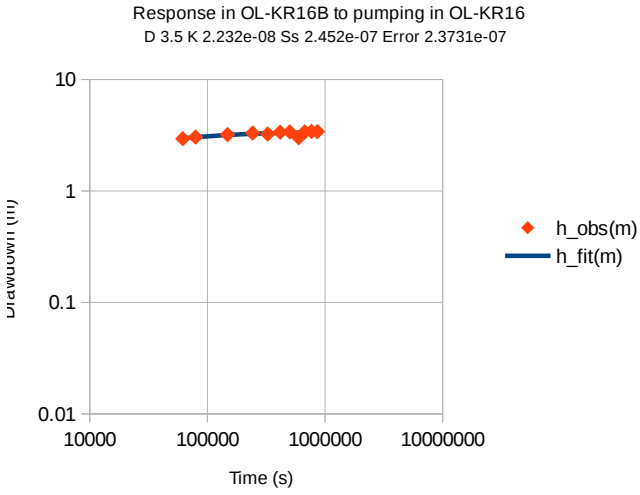
Response in OL-KR16B to pumping in OL-KR16
D 3.5 K 2.232e-08 Ss 2.452e-07 Error 2.3731e-07
10
1
0.1
0.01
Drawdown (m)
10000
100000
1000000
10000000
Time (s)
h_obs(m)
h_fit(m)

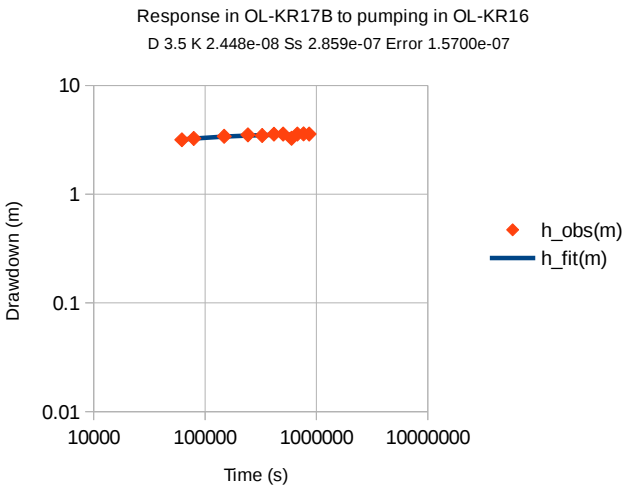
Response in OL-KR17B to pumping in OL-KR16
D 3.5 K 2.448e-08 Ss 2.859e-07 Error 1.5700e-07
Drawdown (m)
Time (s)
h_obs(m)
h_fit(m)

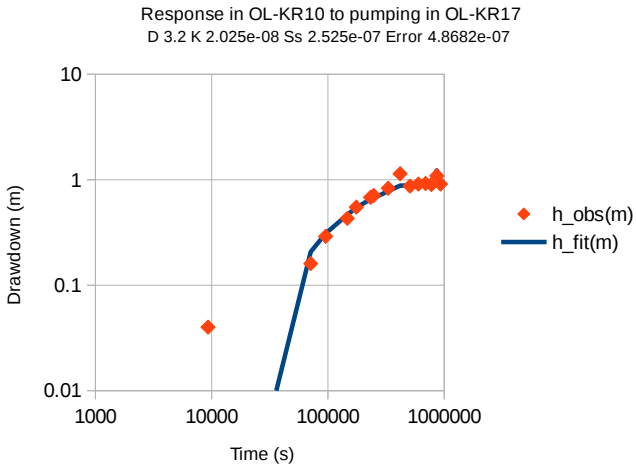
Response in OL-KR10 to pumping in OL-KR17
D 3.2 K 2.025e-08 Ss 2.525e-07 Error 4.8682e-07
Drawdown (m)
Time (s)
h_obs(m)
h_fit(m)

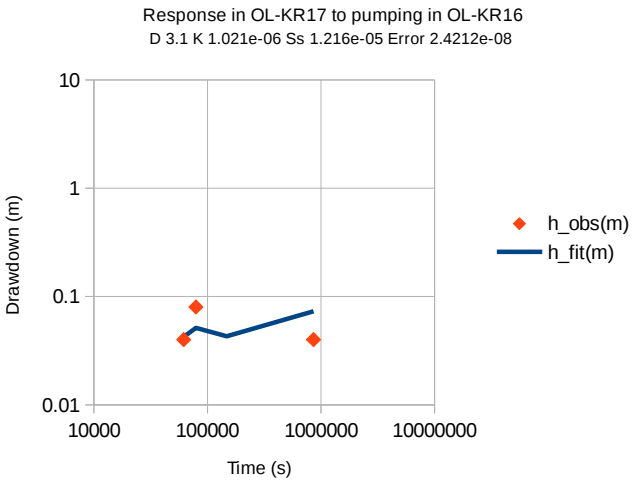
Response in OL-KR17 to pumping in OL-KR16
D 3.1 K 1.021e-06 Ss 1.216e-05 Error 2.4212e-08
Drawdown (m)
Time (s)
h_obs(m)
h_fit(m)

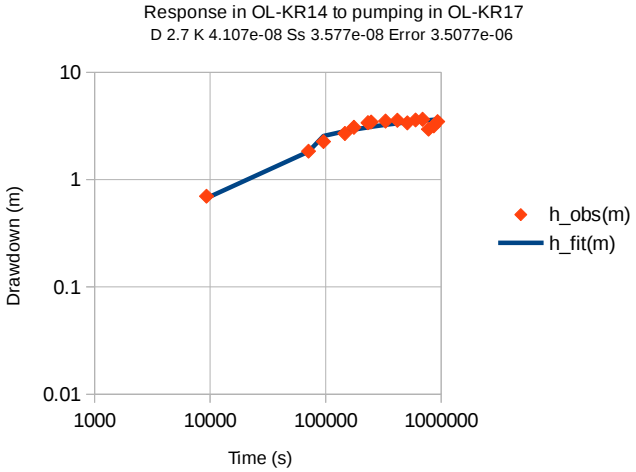
Response in OL-KR14 to pumping in OL-KR17
D 2.7 K 4.107e-08 Ss 3.577e-08 Error 3.5077e-06
Drawdown (m)
Time (s)
h_obs(m)
h_fit(m)

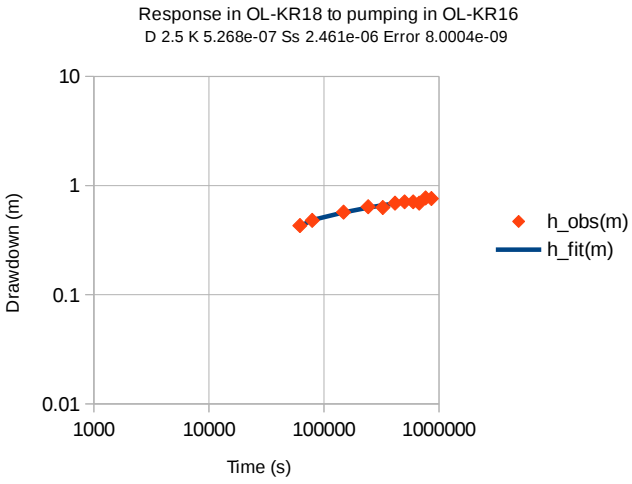
Response in OL-KR18 to pumping in OL-KR16
D 2.5 K 5.268e-07 Ss 2.461e-06 Error 8.0004e-09
Drawdown (m)
Time (s)
h_obs(m)
h_fit(m)

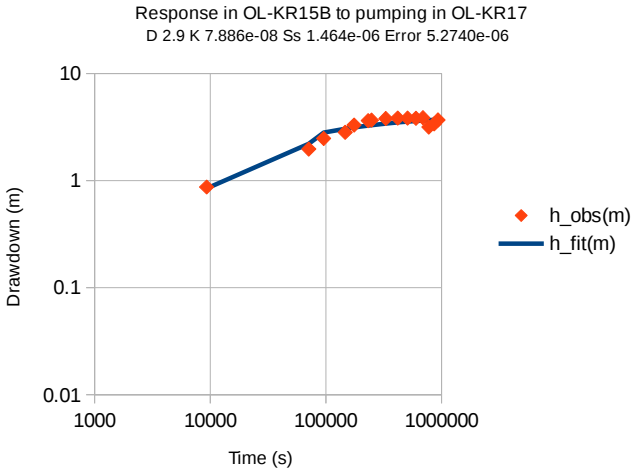
Response in OL-KR15B to pumping in OL-KR17
D 2.9 K 7.886e-08 Ss 1.464e-06 Error 5.2740e-06
Drawdown (m)
Time (s)
h_obs(m)
h_fit(m)

Response in OL-KR15 to pumping in OL-KR17
D 1.8 K 3.595e-06 Ss 2.339e-05 Error 8.1485e-07

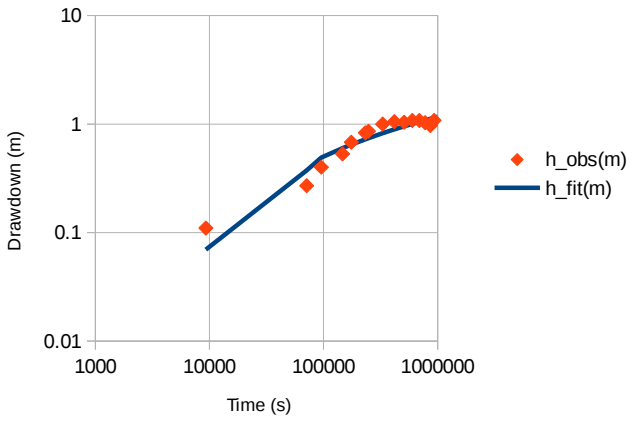

Response in OL-KR18 to pumping in OL-KR17
D 3.5 K 3.161e-08 Ss 2.708e-06 Error 5.9900e-07

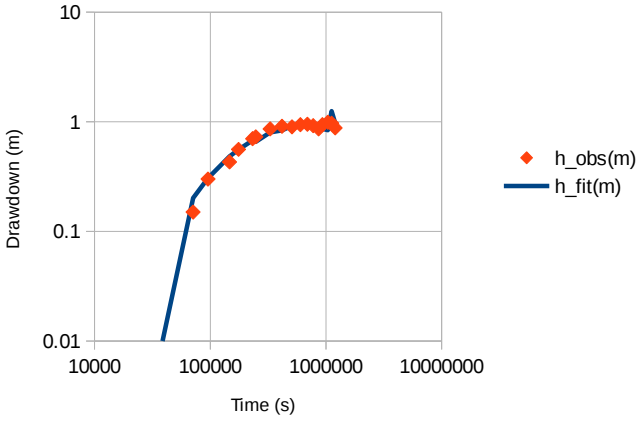

Response in OL-KR16 to pumping in OL-KR17
D 2.1 K 9.200e-07 Ss 5.354e-06 Error 2.4725e-06

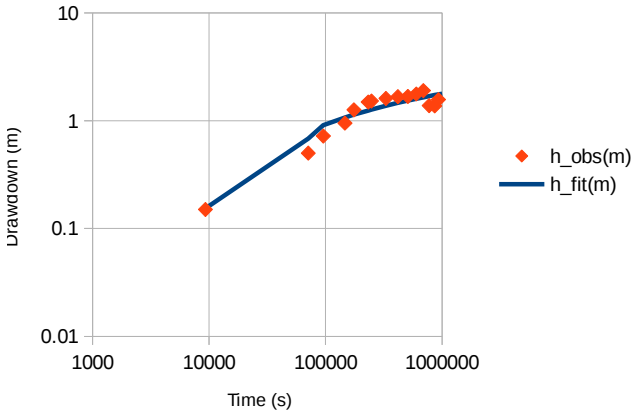

Response in OL-KR10 to pumping in OL-KR18
D 2.6 K 1.407e-07 Ss 2.259e-07 Error 3.7464e-08

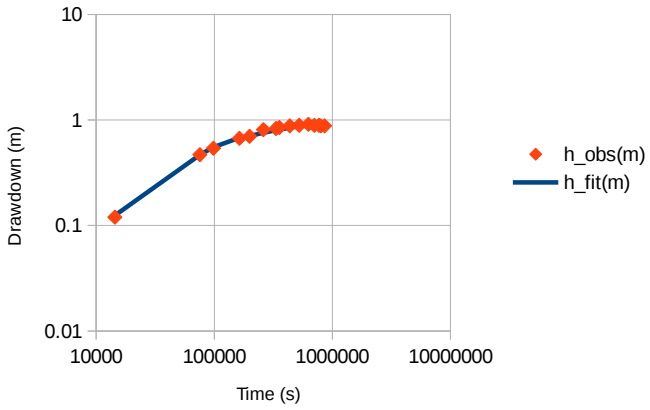

Response in OL-KR17B to pumping in OL-KR17
D 3.1 K 6.788e-08 Ss 1.974e-06 Error 6.5164e-06

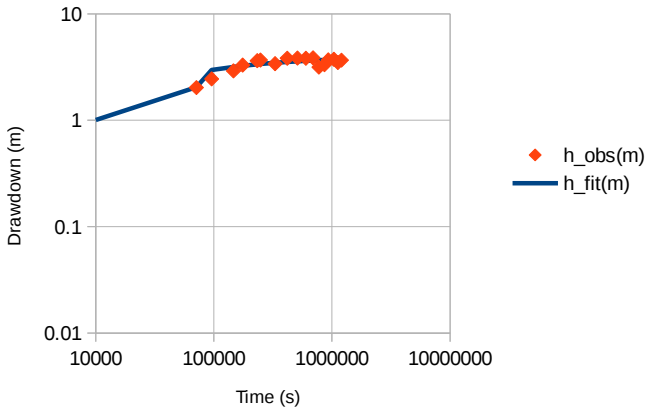

Response in OL-KR14 to pumping in OL-KR18
D 1.8 K 7.929e-06 Ss 1.761e-11 Error 2.8007e-06

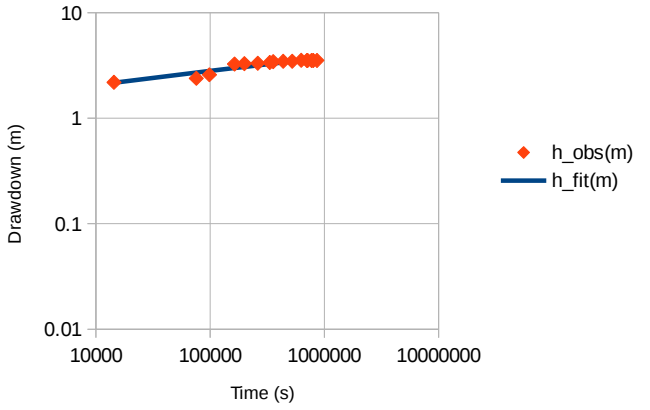

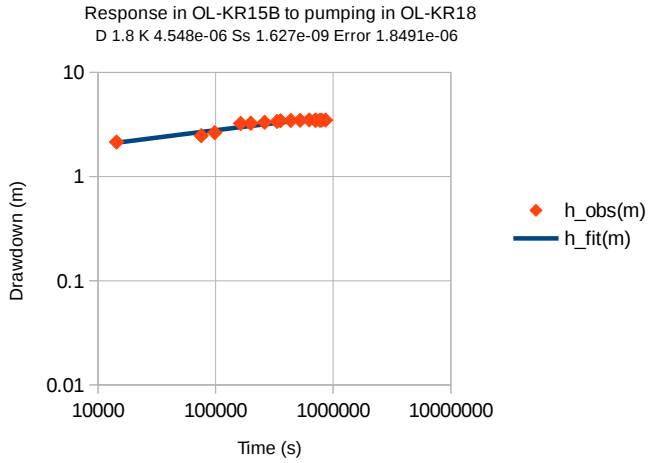
Response in OL-KR15B to pumping in OL-KR18
D 1.8 K 4.548e-06 Ss 1.627e-09 Error 1.8491e-06
Drawdown (m)
10
1
0.1
0.01
10000
100000
1000000
10000000
Time (s)
h_obs(m)
h_fit(m)

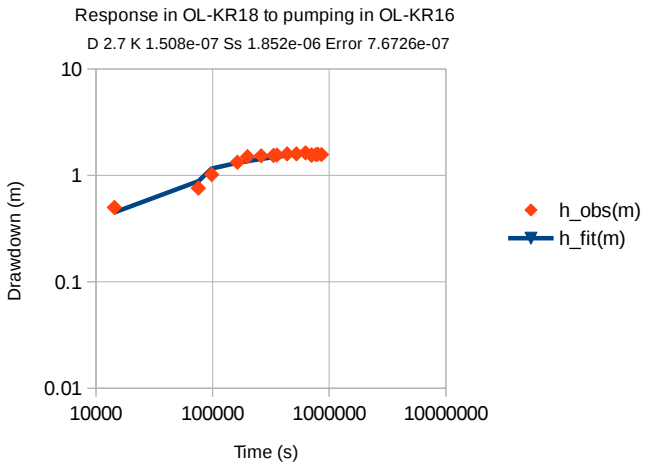
Response in OL-KR18 to pumping in OL-KR16
D 2.7 K 1.508e-07 Ss 1.852e-06 Error 7.6726e-07
Drawdown (m)
10
1
0.1
0.01
10000
100000
1000000
10000000
Time (s)
h_obs(m)
h_fit(m)

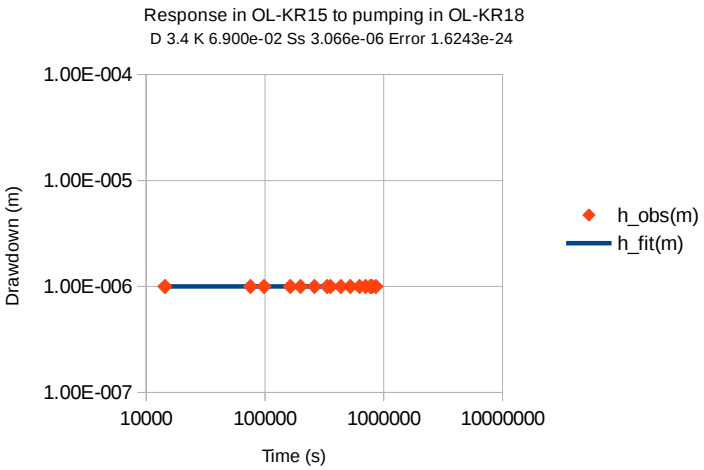
Response in OL-KR15 to pumping in OL-KR18
D 3.4 K 6.900e-02 Ss 3.066e-06 Error 1.6243e-24
Drawdown (m)
1.00E-004
1.00E-005
1.00E-006
1.00E-007
10000
100000
1000000
10000000
Time (s)
h_obs(m)
h_fit(m)

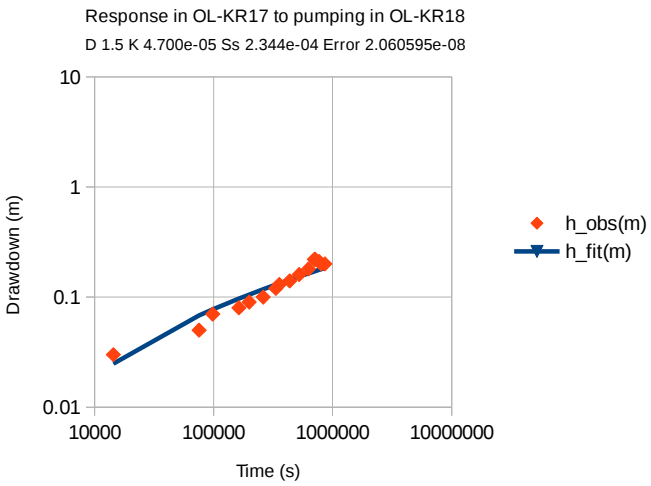
Response in OL-KR17 to pumping in OL-KR18
D 1.5 K 4.700e-05 Ss 2.344e-04 Error 2.060595e-08
Drawdown (m)
10
1
0.1
0.01
10000
100000
1000000
10000000
Time (s)
h_obs(m)
h_fit(m)

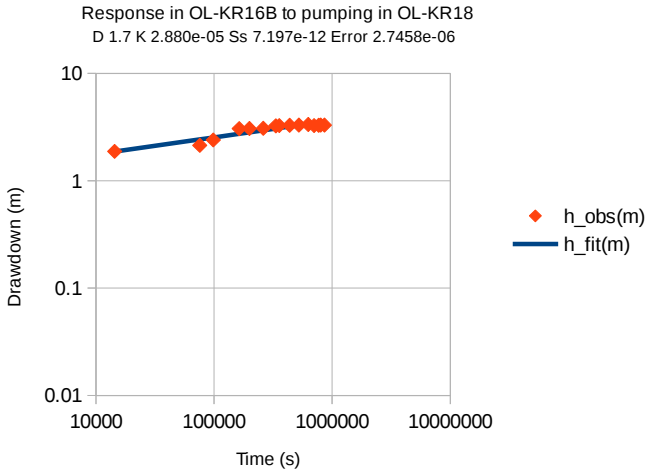
Response in OL-KR16B to pumping in OL-KR18
D 1.7 K 2.880e-05 Ss 7.197e-12 Error 2.7458e-06
Drawdown (m)
10
1
0.1
0.01
10000
100000
1000000
10000000
Time (s)
h_obs(m)
h_fit(m)